LES ANALYSIS OF TURBULENCE GENERATED BY ACTIVE GRID : EFFECT OF WINGLETS AND MOTION PROTOCOL

A Thesis

by

Alper Akardere

Submitted to the
Graduate School of Sciences and Engineering
in Partial Fulfillment of the Requirements for
the Degree of

Master of Science

in the
Department of Mechanical Engineering

Özyeğin University
September 2024

LES ANALYSIS OF TURBULENCE GENERATED BY ACTIVE GRID : EFFECT OF WINGLETS AND MOTION PROTOCOL

Approved by:

Assoc. Prof. Özgür Ertunç
Dept. of Mechanical Eng.
Özyeğin University

Asst. Prof. Altug Melik Basol
Dept. of Mechanical Eng.
Özyeğin University

Prof. Ayşe Gül Güngör
Dept. of Astronautical Eng.
Istanbul Technical University

Date Approved: August 9, 2024

To my family and friends

ABSTRACT

Turbulent flows are one of the most important and challenging phenomena in fluid mechanics. Passive grids are one of the first attempts to create and examine turbulent flows, but their effectiveness in producing higher levels of turbulence is not sufficient. Therefore, active grid designs are emerging with rotating winglet design, which can achieve higher levels of turbulence. This paper reviews different active grid designs and motion protocols. Most of the active-grid studies are experimental.In this paper numerical methods are used and validity of the numerical simulation is checked with several methods, so that the capacity of LESsimulations for the design of active grids can be assessed. The motion of the winglet is one of the most crucial parts of designing an active grid. The most common protocols are random motion and controlled motion. In this paper, a different approach is conducted as an optimized motion where frequency of the rods are optimized with two objective functions. This study examines the relationship between active grid motion and the level of turbulence using several methods.

ÖZETÇE

Türbülanslı akışlar, akışkanlar mekaniğinde en önemli ve zorlu fenomenlerden biridir. Pasif ızgaralar, türbülanslı akışlar oluşturmak ve incelemek için yapılan ilk denemelerden biridir, ancak daha yüksek seviyelerde türbülans üretmede yeterince etkili değildirler. Bu nedenle, döner kanatçık tasarımına sahip aktif ızgara tasarımları ortaya çıkmaktadır ve bu tasarımlar daha yüksek türbülans seviyelerine ulaşabilirler. Bu makale, farklı aktif ızgara tasarımlarını ve hareket protokollerini incelemektedir. Aktif ızgara ile ilgili çalışmaların çoğu deneysel çalışmalardır. Bu çalışmada sayısal yöntemler kullanılmış ve sayısal simülasyonun geçerliliği çeşitli yöntemlerle kontrol edilmiştir, böylece aktif ızgaraların tasarımında LES simülasyonlarının kapasitesi değerlendirilebilmiştir. Kanatçığın hareketi, aktif ızgara tasarımının en kritik parçalarından biridir. En yaygın protokoller rastgele hareket ve kontrollü harekettir. Bu çalışmada, çubukların frekanslarının iki amaç fonksiyonu ile optimize edildiği optimize edilmiş bir hareket olarak farklı bir yaklaşım benimsenmiştir. Bu çalışma, çeşitli yöntemler kullanarak aktif ızgara hareketi ile türbülans seviyesi arasındaki ilişkiyi incelemektedir.

ACKNOWLEDGEMENTS

Firstly, I would like to express my deepest gratitude to my supervisor, Assoc. Prof. zgür Ertunç, for his unlimited support, guidance, and encouragement throughout this journey. I am also immensely grateful to my friend and teammate, Aziz Mert Karul. The countless hours that we have spent working together, brainstorming, and solving problems have been instrumental in the progress of this project. Also, I am glad to have the support of my family, which encourages me in all the processes. Also, I thanks to Asst.Prof.Altuğ Melik Başol and Assoc. Prof. Dr. Ismail Arı for providing computational resources to carry out preliminary numerical simulations and to Özyeğin University for providing HPC cluster.

TABLE OF CONTENTS

LIST OF TABLES

LIST OF FIGURES

GLOSSARY

α_k Initial Phase Difference, p. 8.

A_T Cross-section of test section, p. 8.

A_w Winglet Area, p. 8.

$\beta(t,k)$ Instantaneous Winglet Angle, p. 7.

Co Courant Number, p. 18.

$C(t)$ Instantaneous normalized closure over time, p. 8.

Δ Grid Filter Width, p. 16.

ϵ Turbulent Dissipation Rate, p. 17.

ϵ_{SGS} Sub-Grid Scale Turbulent Dissipation Rate, p. 17.

f_b Resultant Body Forces, p. 15.

$G(r,x)$ Filter, p. 14.

I_c Intensity of Closure, p. 9.

$I_{\langle H \rangle}(x_1, x_2)$ Inhomogeneity Parameter, p. 31.

k Turbulent Kinetic Energy, p. 17.

k_{SGS} Sub-Grid Scale Turbulent Kinetic Energy, p. 17.

λ_g Taylor Microscale, p. 27.

$\langle q^2 \rangle$ Trace of Reynolds Stress, p. 26.

$\langle \overline{U_i(x,t)} \rangle$ Mean Velocity, p. 15.

LES_{IQ} LES Index of Quality, p. 19.

M Winglet Size, p. 7.

μ_t Turbulent Viscosity, p. 15.

ν Dynamic Viscosity, p. 19.

$\nu_{t,eff}$ Effective Viscosity, p. 19.

Ω Rotational Speed, p. 7.

$\overline{p}$ Filtered Pressure, p. 15.

$\overline{U_i}$	Filtered Velocity Field, p. 15.
ϕ	Amplitude of Flapping Angle, p. 8.
$R_{22}(x_1)$	Autocorrelation Function, p. 28.
Re_λ	Taylor Reynolds Number, p. 29.
ρ	Density, p. 15.
Ro	Rossby Number, p. 6.
Ro_m	Mean Rossby Number, p. 9.
T	Stress Tensor, p. 15.
Δt	Time Step, p. 18.
$\tilde{u}_i(x,t)$	Residual Velocity Field, p. 15.
T_q	Turbulent Intensity, p. 25.
U	Velocity, p. 7.
U_{fs}	Freestream Velocity, p. 9.
$u_i'(x,t)$	Fluctuating Velocity, p. 15.
Δx	Mesh Size, p. 18.

CHAPTER I

INTRODUCTION

Turbulence is one of the key aspects of fluid mechanics. Owing to the chaotic motion of fluids in turbulent regime, it is one of few classical physics phenomena whose complex nature and interaction with other phenomena can only be captured with direct numerical simulations and/or complex experiments. Increasing resolution requirements with increasing Reynolds number limit theoretical and numerical studies on turbulent flows. Passive grids are used in the first attempts to create turbulent flows, but high turbulent flows can only be achieved with large high-speed tunnels. Therefore, active grid designs are introduced with rotating rods.

1.1 Static Grid to Active Grid

An early method for designing experimental setups for turbulent flows involves using passive grid designs. Numerous studies have explored passive grids and fractal grids, with notable contributions from Comte-Bellot and Corrsin [1], Thormann and Meneveau [2], and Valente and Vassilicos [3]. Paolo D'Addio et al. [4] discuss the effect of boundary conditions on flow with passive and fractal grids. Ertunc et al. [5] investigate the homogeneity of turbulent flows with static grids. Although passive grids are effective in generating turbulent flows, there are cases where higher turbulence levels are desired. Makita [6] states that large wind tunnels are typically used to achieve high Taylor-Reynolds numbers, but these facilities are costly to operate and have experimental challenges. Therefore, active grid designs were developed to achieve these goals. The main difference between active and passive grids is the motion of the winglets. In passive grid designs, there is no motion, and higher levels of turbulence cannot be obtained. In active grid designs, winglets can be controlled with motors to enhance turbulent structures. Additionally, Bewley et al. (2020) mentioned that high Reynolds numbers can be achieved with smaller wind tunnels. Makita (1991) was one of the first to design an active grid. The effects of active and passive grids can be categorized as excited and non-excited turbulent flows. Excited turbulence is stronger than non-excited turbulence in terms of turbulent quantities. In the Makita design, the winglets are connected to horizontal and vertical rods, which can be individually rotated by motors.

1.2 Different Active Grid Designs

Several different designs of active grids were conducted. These designs were carried out for different reasons, such as increasing the durability of the structure, a decrease in the pressure drop caused by the active grid and an increase in velocity fluctuation. In Reinke et al.[7] , an active grid was designed called a low blockage active grid design. In this design there is a 90 degree phase difference between vertical and horizontal rods. Reinke et al.[7] mentioned that total blockage over time should not be changed instantly. Instantaneous changes in blockage cause extreme loads on the structure and cause fatal damage to the wind tunnel structure. One of the significant differences between the Makita design and the Reinke design is the type of rod connection. In the case of Makita design, full rods are used and grids are placed on rods. In low blockage design, the winglet-to-winglet rod type is used. The minimum blockage over time decreased from 20 % to 6 %. This change is crucial for high-speed wind tunnels. Low blockage causes a low pressure drop caused by an active grid. In addition, the blockage range increases as the minimum blockage decreases. In Hearst and Lavoie [8], different types of grid layout are used. In this design, adjacent winglets are located on different rods. Therefore, decoupled winglets can increase random spatial sequence more than traditional winglets. In addition, Skeledzic et al. [9] implemented various degrees of freedom that can be achieved by implementing servomotors in each winglet.

Most active-grid investigations are experimental studies. Kang et al. [10] conducted one of the few numerical investigations.

Skeledzic et al. [9] and Griffin et al. [11] controlled each winglet by servo motors separately to achieve high Reynolds number. In addition, circular holes were applied to the winglets. This allows both minimizing maximum blockage of the active grid and creating smaller scales of turbulent fluctuations. Neuhaus et al. [12] investigated the effect of variations in active grid blockage on the resulting flow. Shafts are separated into 2 different groups to control the blockage over time and keep blockage over time constant. The adjacent rods are rotated in different directions. Neuhaus et al. [12] claimed that constant blockage over time allows one to assume a constant load on the fan. Kevin P. Griffin et al. [11], discuss correlated motions of grids. Velocity fluctuations and Reynolds number are manipulated by changing the motion of the grid.Gregory P. Bewley et al. [13] offer a distinct design perspective on active grids, employing individual motor control for each winglet in their study. L. Mydlarski et al. [14] aimed to achieve similar conditions in oceans and atmosphere without the effect of shear.

1.3 Motion of the Rods

There are different techniques for creating angular velocity signals. Those are random motion and controlled motion. In random motion, frequencies are randomized. In controlled motion, there is dependency on the motion of the rods. Hearst et al. [8] suggested that there is no major difference between controlled motion and randomized motion. However, Griffin et al.[11] suggested that adding correlation to rods makes fluid motion more correlated. Hearst et al. [8] and Griffin et al. [11]achieved different results in turbulence statics between controlled and randomized motion, but both find that controlled motion causes a less homogeneous flow field. The difference in correlation of flow and active grid, is a result of different active grid designs. In

Griffin et al. [11] each winglet is controlled by a different servo motor. In Hearst et al. [8] the winglets are mounted on a single rod. It is not possible to reach as much as flow, active grid correlation of independent winglets, with mounted winglet design. In this project winglets are mounted on rods. Although the main motion protocols are random motion and controlled motion, in this paper an optimized motion protocol is used to control the closure over time. In addition, flapping motion is selected rather than constant angular velocity to achieve higher levels of turbulence.

1.4 Open Fields in the Literature

In literature there are lots of experimental studies on active grid.There are not any numerical studies for active grid. More information from flow field can be gathered with numerical simulation but in shorter time.Therefore, lots of different statistical calculations can be made. Also, in literature either randomized or controlled motion protocols are used. In this study optimized motion is used. Therefore, control over grid motion is increased and relation between grid motion and flow field can be analysed more systematically.

1.5 Hypothesis of the Study

In most of the studies random motion or controlled motion is used.Using optimized motion by genetic algorithm increases control over active grid.Therefore, control over flow field is increased.Also, effect of different winglet shapes should effect flow field in different aspects.

1.6 Objectives of the Study

This thesis emphasises numerical methods to analyze active grid results. In this study, only a portion of the active grid is simulated to decrease desired computational power but it should be large enough to observe effect of optimized motion effects. The main parameters of the active grid are the shape, size, and motion protocol of the winglets. This study explores the effects of square and circular winglets on turbulent quantities, flow isotropy, and flow homogeneity, as well as the influence of different motion protocols.

1.7 Methodology

There are several crucial parameters for designing active grid structure. Those are winglet shape, winglet size, inlet velocity and motion of the rods. Two different winglet shapes are selected as circular and square winglets. While determining motion of the rods genetic algorithm optimization is used for finding suitable motion. Motion of the winglet should create high level of turbulence and instantaneous pressure change should be minimized. Star-CCM+ is used for numerical study.LES method is used for examining turbulent structures more accurately. Results are obtained from both point probes and planes. Calculations are made in MATLAB software.

CHAPTER II

ACTIVE GRID DESIGN AND MOTION PROTOCOL

2.1 Grid Design and Layout

In this study, the active grid is analyzed for wind tunnel application. It is placed at the entrance of the test section of the wind tunnel that has a cross section area of 2.2 x1.7 m^2. Winglet size, motion protocol and winglet layout are the most important design parameters of the active grid turbulence generator. In determining winglet size and motion protocol, the Rossby number is used. Rossby number is the ratio of the free stream velocity to the mesh length times the rotational speed.In this study the free stream velocity equals 1 m/s. Hearst (2015) suggested keeping the Rossby number below 50. After $Ro = 50$ there is no important change in turbulence intensity. The size of the wings is determined to be 15 cm. Therefore, there are 9 horizontal rods and 12 vertical rods in the active grid.

The rods are rotated with flapping motion and the angular motion is a sinusoidal wave with optimized frequencies. In Reinke [7] the low blockage design is recommended for a more reliable and safe design. Also, the blockage change should not be instantaneous. This approach is applied in an active grid. There is a 90-degree shift between the horizontal and vertical rods at the initial position. In addition to this approach, in this project the vertical and horizontal rods are separated by a distance of 2M (M = 0.15m). Although a low-blockage design is implemented, there can be a blockage problem in instant changes. This situation is not problematic for experimental setups, but in numerical simulations, instantaneous closure change causes a rapid change in momentum. Rapid increase in pressure crashes numerical simulation and results are not reliable. To eliminate this problem, vertical and horizontal rods

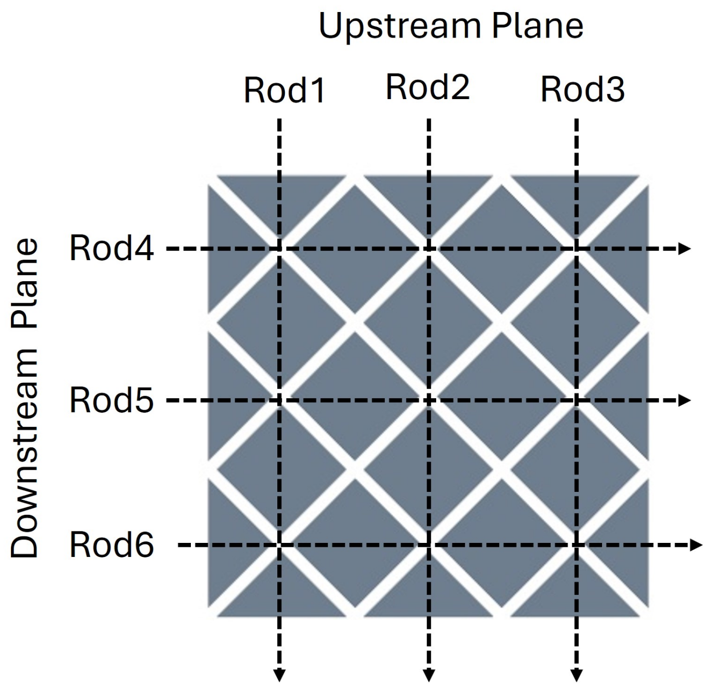

Figure 1: Active Grid Layout

are separated. Also, 2 different winglet shapes are implemented as square and circle.

$$Ro = \frac{\langle U \rangle}{\Omega M} \tag{1}$$

where $\langle\ U\ \rangle$ is mean velocity, Ω is rotational speed and M is winglet size.

2.2 Motion Protocol

In this section, the motion protocol is implemented. As mentioned, in most studies random motion and controlled motion are used. In this paper, an optimized motion is introduced. The motion protocol is determined by two objective functions.Then, the rotational frequency of the wings is determined by an optimization process. For this purpose, an instantaneous winglet angle is calculated.

The instantaneous angle of the winglet of the rod k^{th}, which is denoted by $\beta(t, k)$, is defined by the superposition of two rotation frequencies with the same amplitude as follows:

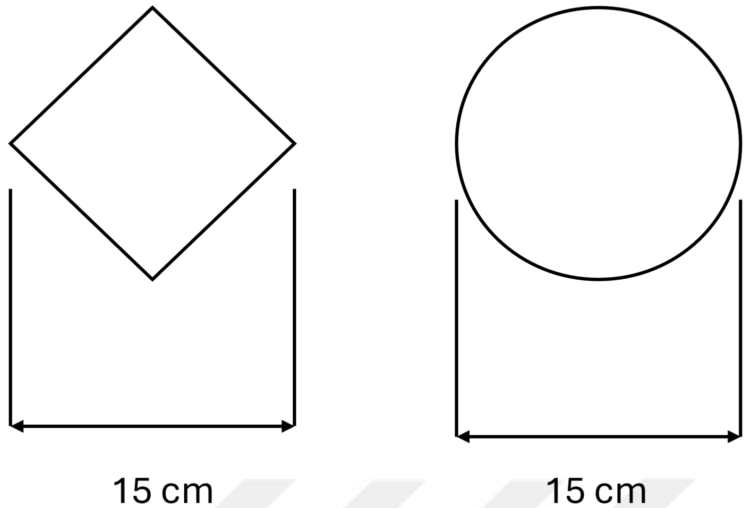

Figure 2: Winglet Types

$$\beta(t,k) = \alpha_k + \frac{\phi}{2}(sin(2\pi f_{k,1}t) + sin(2\pi f_{k,2}t)) \tag{2}$$

where α_k is the initial phase difference, ϕ is the amplitude of the flapping angle, which is maintained at 90° for all rods, and t is time. The subscripts 1 and 2 correspond to two different frequencies of the k-th rod. The initial phase difference of vertical and horizontal rods is 0° and 90°, respectively. Hence, only $f_{k,1}$ and $f_{k,2}$ are determined via optimization for a required mean Rossby number and intensity of area closure.

The instantaneous normalized closure over time,$C(t)$, is defined as follows:

$$C(t) = \sum_{k=1}^{N} \frac{mA_w sin(\beta(t,k))}{A_T} 100 \tag{3}$$

where N is number of rods, A_w is winglet area, m is number of winglets on single rod, and A_T is total area of test section.

Closure over time is an important parameter for both active grid design and turbulence. As mentioned in Reinke (2017) instant changes in closure over time can cause problems because of instantaneous pressure change. In contrast, increasing the fluctuations of the closure over time helps to achieve higher levels of turbulence. Therefore, the average closure over time should be minimized to decrease instant changes in pressure drop, but fluctuations should also be increased to maximize turbulence statistics. For this purpose, the first optimization objective is introduced as the intensity of closure.

$$I_c = \sqrt{\frac{\int (C(t) - \langle C(t) \rangle)^2 dt}{N}} \cdot \frac{1}{\langle C(t) \rangle} \tag{4}$$

where N is total number of samples,C(t) is closure over time,T is final time , $\langle C(t) \rangle$ is mean of closure over time and I_c is intesity of closure.

In most of the studies, the Rossby number is constant for all the rods but in this paper all rods are moving in different signals with flapping motion. Therefore, each rod has a different Rossby number, and the Rossby number of each rod changes with time. Instead of assigning constant Rossby number, changing Rossby number is averaged in both time and rods. Hence, the second objective function for optimization becomes the mean Rossby number.

Since the flapping motion is selected, the instantaneous velocity of the winglets changes with time. Therefore, the mean winglet angular velocity should be determined for the Rossby number calculation as shown in Equation 5. In the first step, the angular velocity by time is calculated by taking the derivative of the winglet angle by time. Since the angular velocity can be both positive and negative, the absolute angular velocity is calculated. Then, the mean of this term is calculated.

$$\Omega_M(k) = \langle \left| \frac{d\beta(t,k)}{dt} \right| \rangle \tag{5}$$

$$Ro_m = \frac{1}{N} \sum_{k=1}^{N} \frac{U_{fs}}{M \Omega_M(k)} \tag{6}$$

where U_{fs} is freestream velocity at inlet, M is winglet size, N is number of rods and Ro_m is mean Rossby number.

Closure intensity and mean Rossby number are defined as optimization objectives. Frequencies can be optimized with these parameters. In this paper, 2 different cases

Table 1: Rossby number of each rod and mean Rossby number for two optimized motion protocols for $I_c = 0.15$ and $I_c = 0.13$

k(Rod Number)	Rossby Number	Rossby Number
1	17.4	80.5
2	37.9	24.6
3	28.4	34.3
4	17.3	61.2
5	24.3	24.5
6	16.2	25.8
Ro_m	23.6	41.8

are investigated for 23.6 and 41.8 mean Rossby for both square and circular winglets. In addition, the closure intensity is selected as 0.15. The optimal Rossby number value can be seen in Table 1.

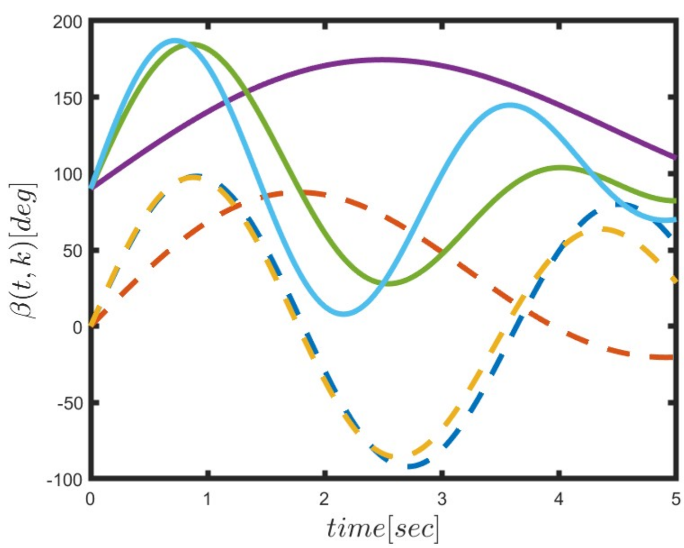

Figure 3: Angular positions of rods with $Ro_m = 41.8$ and $I_c = 0.15$ where the continuous line shows horizontal rods and dashed line shows vertical rods

In Figure 3 and Figure 4 the angular position of the rods can be seen for the mean Rossby number of 23.6 and 42.8 and the closure intensity of 0.15. The major difference between these results is the frequency of the waves.The angular velocity term in the Rossby number is in the denominator. In addition, in this paper the active grid is separated into two layers. Initial position of layer 1 is 0 degree and

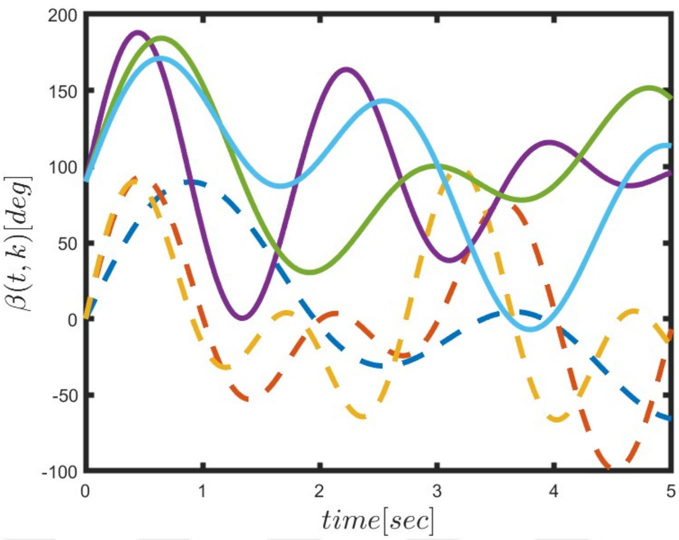

Figure 4: Angular positions of rods with $Ro_m = 23.6$ and $I_c = 0.13$ where the continuous line shows horizontal rods and dashed line shows vertical rods

initial position of the layer 2 is 90 degree.

In figure 5 closure over time can be seen for the mean Rossby numbers 23.6 and 41.8 and the closure intensity 0.15. As mentioned in Reinke(2017), closure changes should not be rapid and should be as smooth as possible. Also, closure changes should create strong turbulent levels.In this paper, the goal intensity is 0.15 for both 25 Rossby case and 40 Rossby case.Even though the angular positions of two cases are quite different, their closure over time graph is similar to each other.

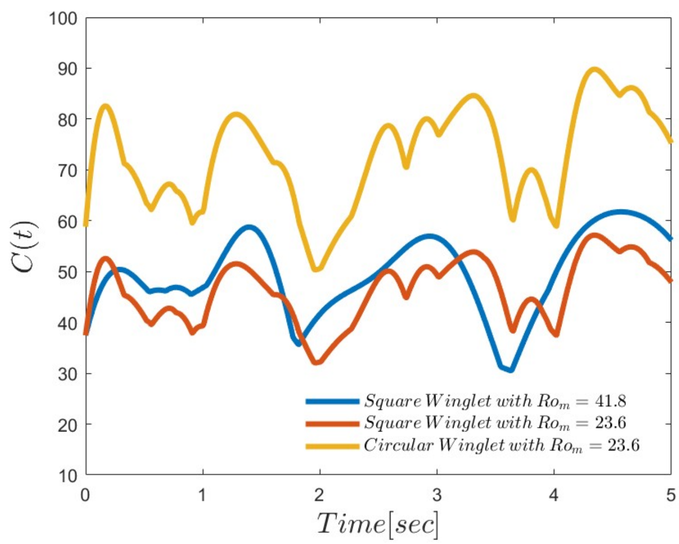

Figure 5: Closure over time for both Ro=23.6 and Ro=41.8 where continous line represent square winglets, dashed line represent circular winglet

CHAPTER III

NUMERICAL SETUP

StarCCM + software is used to simulate active grid-generated turbulence.In this paper, square and circular winglet geometries are simulated. There are two different regions in the simulation cylindrical domain which involve winglets and the rest of the domain. In hardware design there are 9 horizontal and 12 vertical rods but to decrease computational time, 3 by 3 vertical and horizontal rods are modeled with periodic conditions at the side boundaries. In mesh operation, the trimmer mesh is selected. The mesh size of the numerical analysis is that the maximum mesh is 0.005 m and the minimum cell size is 0.0005 m. The mesh scene can be seen in Figure 7. In the case of models, coupled flow is selected and a bounded central differencing method is implemented with a blending factor of 0.15 upwind. In addition, the $2^n d$ order temporal discretization is selected for a more accurate solution with 0.001 second.

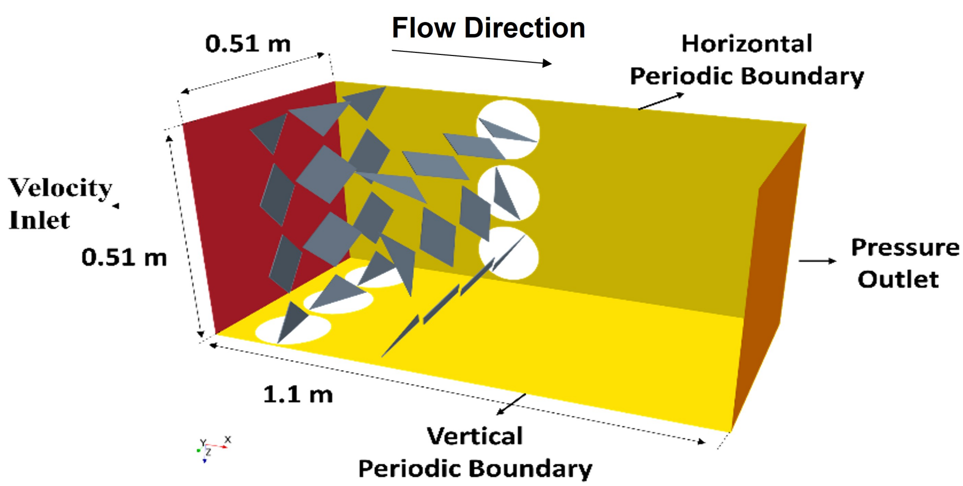

Figure 6: Dimensions and boundary conditions of active grid geometry

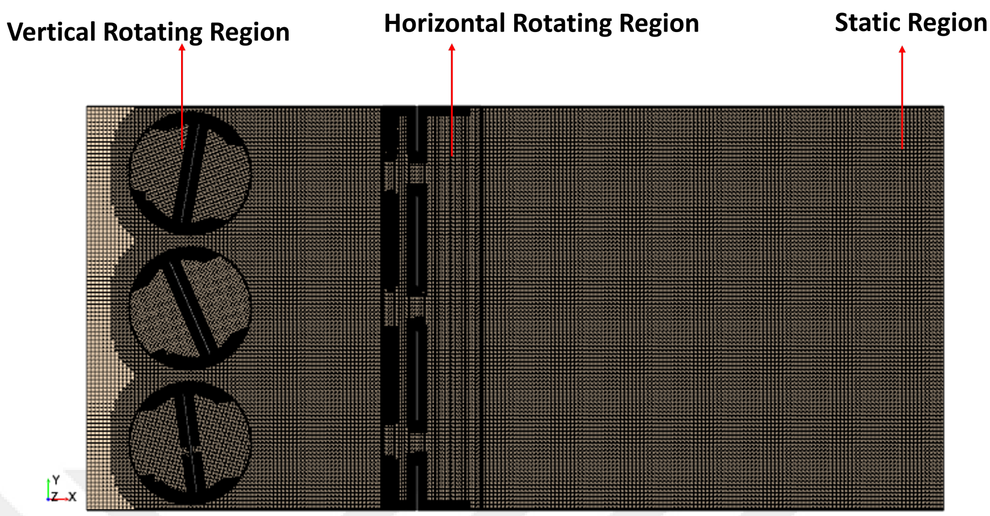

Figure 7: Mesh scene from midplane of the domain

3.1 Numerical Model

There are several simulation methods that can be used such as DNS,LES and RANS models. DNS simulations are the most accurate among them, but complexity of the geometry and high Reynolds number increase the computational time of DNS analysis dramatically. The computational cost of DNS analysis increases with the Reynolds number cube[15]. In addition, Reynolds stress models are using models such as k-ϵ and k-ω. LES model relies on the DNS and RANS models. Pope[15], states that the DNS method uses most of the effort in dissipative motions, but most of the energy is contained in larger eddies. In the LES method, larger eddies are computed explicitly and smaller eddies are modeled. In the LES method, the velocity is filtered with a cut-off frequency. Then, the velocity field can be decomposed into filtered velocity field and residual velocity field with Leonard's decomposition[16, 17]. Filtered velocity can be described as:

$$\overline{U_i}(t,x) = \int G(r,x)U_i(x-r,t)dr \tag{7}$$

where $G(r,x)$ is filter, ,and $U(x-r,t)$ is velocity fields.

In Star-CCM+ implicit filtering is used. The size of the computational grid determines the size of the eddies that are filtered out. Decomposed velocity can be composed into:

$$U_i(x,t) = \tilde{u}_i(x,t) + \overline{U_i}(x,t) \tag{8}$$

where $\tilde{u}_i(x,t)$ is residual velocity field and $\overline{U_i}$ is filtered velocity field.

Then, the filtered velocity is separated into mean velocity and fluctuating velocity with Reynolds decomposition[18] as:

$$\overline{U_i}(x,t) = \langle\overline{U_i(x,t)}\rangle + u_i'(x,t) \tag{9}$$

where $\langle\overline{U_i(x,t)}\rangle$ is mean velocity and $u_i'(x,t)$ is fluctuating velocity

In the next step, decomposed velocity inserted into mass and momentum equation.

$$\nabla.(\rho\overline{U}) = 0 \tag{10}$$

$$S = \frac{1}{2}(\nabla\langle\overline{U}\rangle + \nabla\langle\overline{U}\rangle^T) \tag{11}$$

$$T_{SGS} = 2\mu_t S - \frac{2}{3}(\mu_t\nabla.\overline{U})I \tag{12}$$

$$\frac{\partial}{\partial t}(\rho\overline{U}) + \nabla.(\rho\overline{U}\otimes\overline{U}) = -\nabla.\overline{p}I + \nabla.(\overline{T} + T_{SGS}) + f_b \tag{13}$$

where $\overline{U}$ is filtered velocity field, ρ is density, $\overline{p}$ is filtered pressure and T is stress tensor, f_b is resultant body force, μ_t is turbulent viscosity.

In Star-CCM + software there are 3 subgrid scale models that can be used. In this paper WALE subgrid model is selected.Wale subgrid scale model defines subgrid viscosity as defined as[19] :

$$\mu_t = \rho(C_m\Delta)^2\frac{(S_{ij}^d S_{ij}^d)^{3/2}}{(\overline{S_{ij}S_{ij}})^{5/2}(S_{ij}^d S_{ij}^d)^{5/4}} \tag{14}$$

$$S_{ij}^d = \frac{1}{2}((\overline{g}_{ij})^2 + (\overline{g}_{ji})^2 + \frac{1}{2}\delta_{ij}(\overline{g}_{kk})^2 \tag{15}$$

$$\overline{S_{ij}} = \frac{1}{2}(\frac{\partial \overline{U_i}}{\partial x_j} + \frac{\partial \overline{U_j}}{\partial x_i}) \tag{16}$$

$$\overline{g}_{ij} = \frac{\partial \overline{u_i}}{\partial x_j} \tag{17}$$

$$\overline{g}_{ij}^2 = \overline{g}_{ik}\overline{g}_{kj} \tag{18}$$

where ρ is the density, C_m is constant and Δ grid filter width or length scale. Δ is defined in terms of cell volume. It can be defined as:

$$\Delta = C_w V^{1/3} \tag{19}$$

where C_w is model coefficient which equals 0.544 and V is cell volume.

3.2 Accuracy of the Numerical Simulation

Although the LES method is quite feasible, the quality of the simulation has to be checked. There are several methods that can be used to assess simulation quality.Resolved kinetic energy and resolved dissipation are one of them. In order to calculate resolved values, k_{SGS} and ϵ_{SGS} have to be defined:

$$k_{sgs} = C_t \frac{\mu_t}{\rho} S \tag{20}$$

$$\epsilon_{sgs} = \frac{\mu_t}{\rho} S^2 \tag{21}$$

$$\epsilon = \nu(\frac{\partial \overline{U_i}}{\partial x_j} + \frac{\partial \overline{U_j}}{\partial x_i})\frac{\partial \overline{U_i}}{\partial x_j} \tag{22}$$

$$q^2 \equiv \langle u_i' u_i' \rangle \tag{23}$$

$$k = \frac{1}{2}\langle q^2 \rangle \tag{24}$$

Then, the resolved kinetic energy and resolved dissipation can be defined:

$$R_k = \frac{k}{k + k_{SGS}} \tag{25}$$

where k is turbulent kinetic energy and both averaged in plane and time, k_{SGS} is subgrid scale turbulent kinetic energy and averaged in plane.

$$R_\epsilon = \frac{\epsilon}{\epsilon + \epsilon_{sgs}} \tag{26}$$

where ϵ is dissipation rate and averaged in time, ϵ_{SGS} is subgrid scale dissipation rate averaged in time

In figure 12 and figure 13 the resolved turbulent kinetic energy and the resolved dissipation rate of the square and circular winglets can be seen. There is a major difference between R_k and R_ϵ. When R_k and R_ϵ are compared in X / M = 5 with square winglets, the mean R_k is 97 % and the mean R_ϵ is 64 %. The differences between those values are similar for other positions and winglet types. This difference is caused by length scales associated with turbulent kinetic energy and dissipation rate. The energy is mainly contained in larger eddies, while the dissipation rate is related to small-scale eddies. As mentioned before LES analysis larger eddies is computed explicitly and smaller eddies are modeled. Therefore, most of the kinetic energy is already computed explicitly, and a small part of it is modeled. In contrast, most of the dissipation rate is modeled with subgrid scale models. The results show that R_k is not much affected by the distance to the grid, but R_ϵ is much more dependent on the distance to the grid. In the next step, the quality of the mesh is controlled with the parameters of LES_{IQ} and Courant number. The courant number calculation was performed for the resolution, velocity, and time step selection of the mesh. Courant number,Co, defined as[20]:

$$Co = \frac{U\Delta t}{\Delta x} \tag{27}$$

where U is velocity, Δt is time step and Δx is mesh size

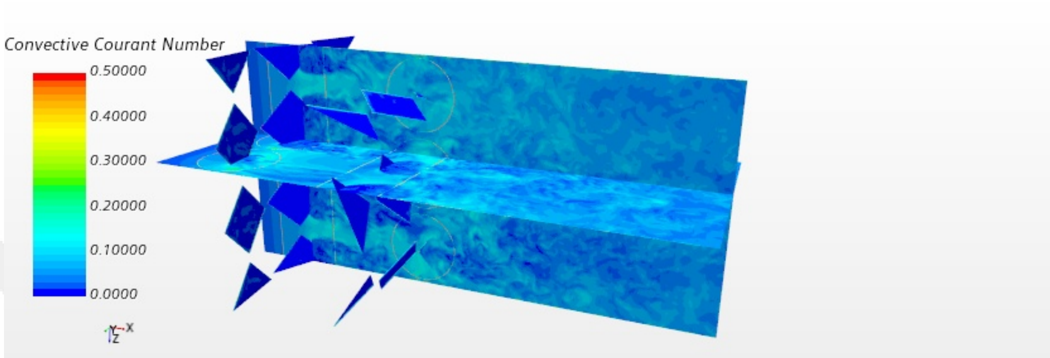

Figure 8: Courant number of the simulations for square winglets at $Ro_M = 23.6$

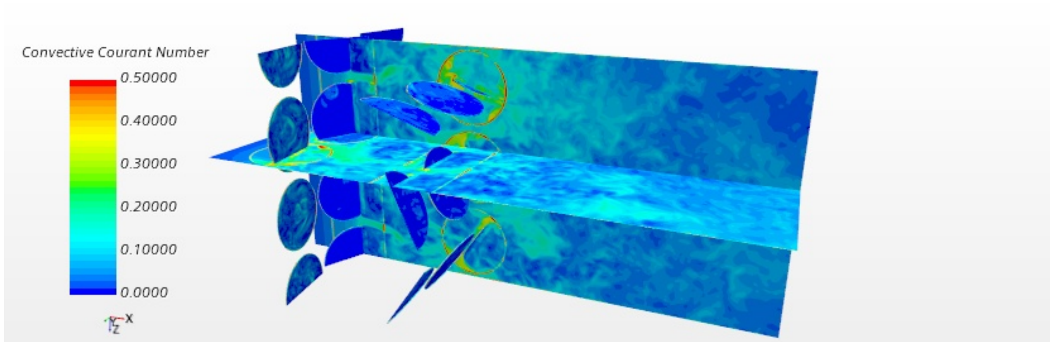

Figure 9: Courant number of the simulations for circular winglets at $Ro_M = 23.6$

In figure 9 and figure 8 Courant number distribution in both square and circular winglets can be seen. The Courant number should be less than 1 for a reliable numerical analysis. Therefore, both square and circular winglet results are acceptable for Courant number.

In the next method, the value LES_{IQ} is evaluated. LES_{IQ} is a parameter to show the quality of the LES analyze. The value should be greater than 0.8 to have realable analysis results[21].

$$LES_{IQ} = \frac{1}{1 + 0.05 \frac{\nu_{t,eff}}{\nu}^{0.53}} \tag{28}$$

where $\nu_{t,eff}$ is effective viscosity and ν is dynamic viscosity.

In figures 10 and 11 the results of LES_{IQ} can be seen.

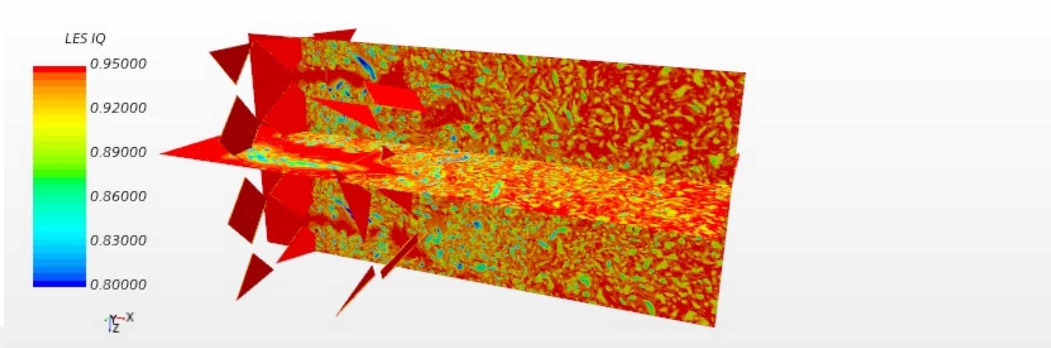

Figure 10: LES IQ of the simulations for square winglets at $Ro_M = 23.6$

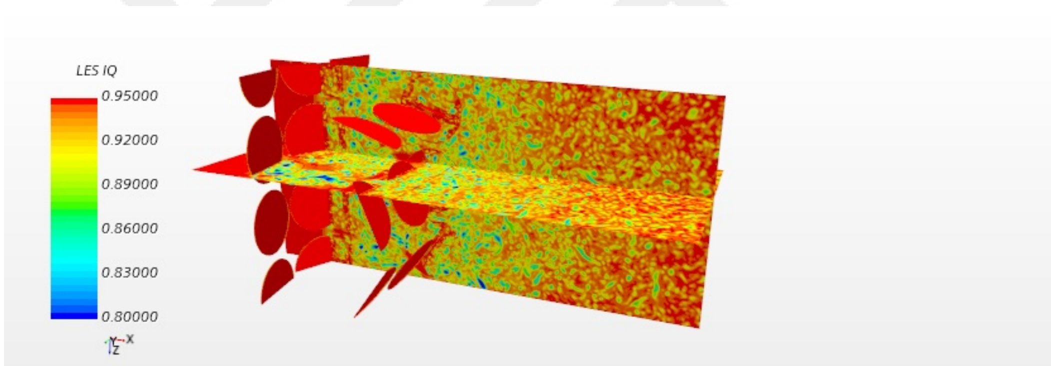

Figure 11: LES IQ of the simulations for circular winglets at $Ro_M = 23.6$

LES_{IQ} is an important parameter for the quality of the simulation.It should be higher than 0.8 for a realible simulation. In figures 11 and 10 the results of the circular and square wings can be seen. In most of the domain LES_{IQ} the value is almost 0.9.It is 0.8 only near the winglet. It is acceptable for a valid simulation.

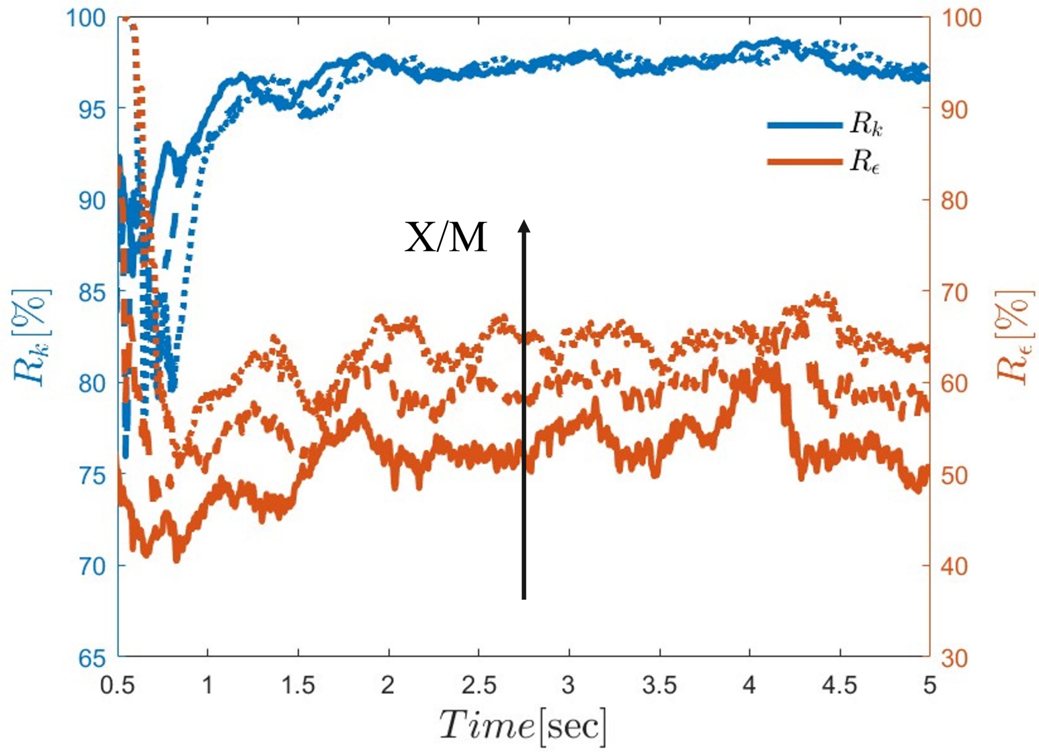

Figure 12: Resolved turbulent kinetic energy and resolved dissipation with square winglets

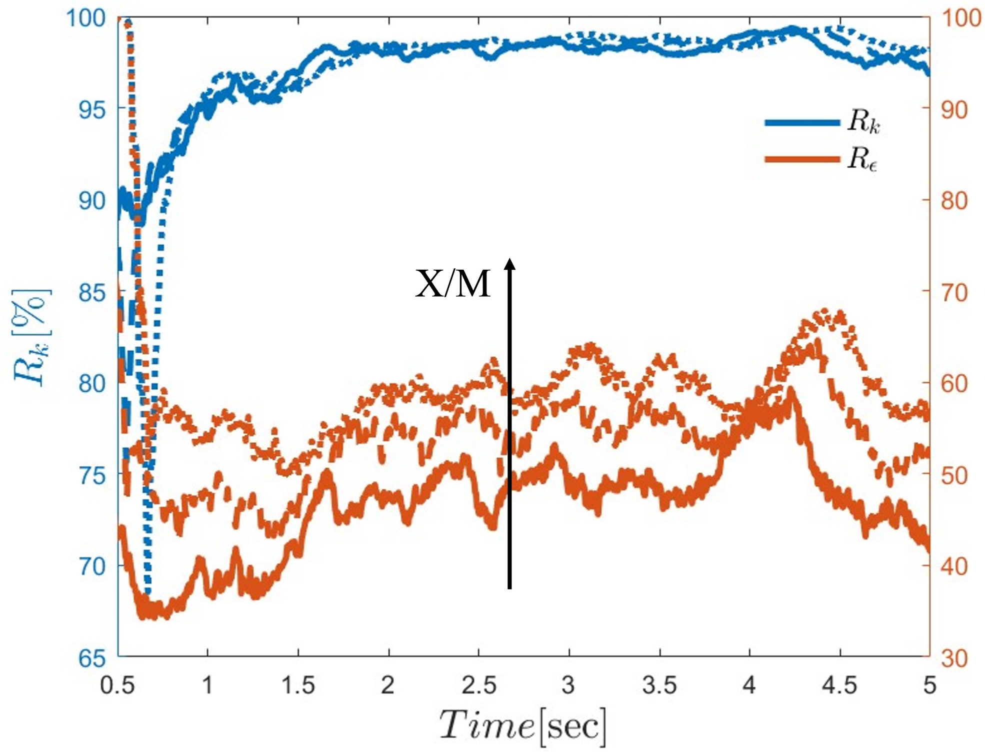

Figure 13: Resolved turbulent kinetic energy and resolved dissipation with circular winglets

CHAPTER IV

ISOTROPY OF THE FLOW

In this section, the isotropy level of the flow is evaluated.Kang(2003) measured the global isotropy level from X/M = 20 to X/M = 48. The mean global isotropy level is found at 1.1 and deviates by 15% [10]. Hearst (2015) measured the global isotopy level at X/M = 30 with various Rossby numbers. When the Rossby number increases to 200, the global isotropy level increases from 1.1 to 1.7 [8]. Mydlarski & Warhaft (1996) measured the global isotropy level in X/M = 68 and found 1.21[14].

In Figure 14 the Reynolds stress change in the test section can be seen for both square and circular winglets. Results are shown. It can be seen that circular winglets have higher Reynolds stress in each component compared to square winglets. The effect of the winglet shape is higher than the motion protocol in the case of Reynolds stress. In addition, the $\langle u_3 u_3 \rangle$ component is higher than the other component in all winglet shapes and motion protocols. This effect is caused by the placement of horizontal and vertical layers. The final layer rotates around x_2. Therefore, it creates fluctuations around x_3. Therefore, it can be expected to have a higher Reynolds stress in $\langle u_3 u_3 \rangle$.

In figure 15 global isotropy level can be seen in both different motion protocols and winglet shapes. The global isotropy level changes between 1.15 and 0.9 at $X/M = 3$. Also, it changes between 1.1 and 0.7 at $X/M = 5$. Both $\sqrt{\langle u_1^2 \rangle / \langle u_2^2 \rangle}$ and $\sqrt{\langle u_1^2 \rangle / \langle u_3^2 \rangle}$ are considered. Square wiglets provide more isotropic flow in both motion protocols to circular winglets.

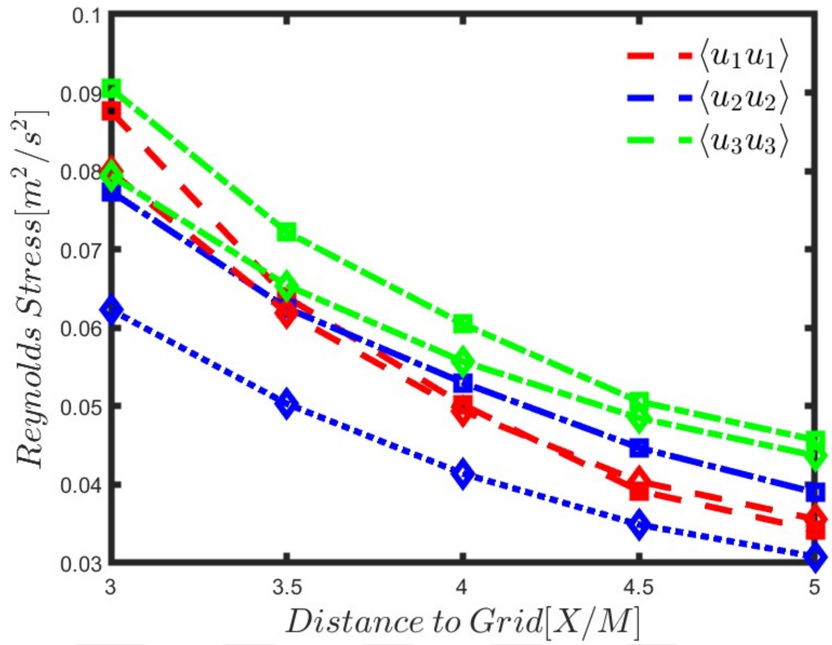

Figure 14: Reynolds stress changes over distance to grid where circle sign denotes circular winglet at $Ro_m = 23.6$,square sign denotes square winglet at $Ro_m = 23.6$ and diamons sign denotes sqaure winglet at $Ro_m = 41.8$

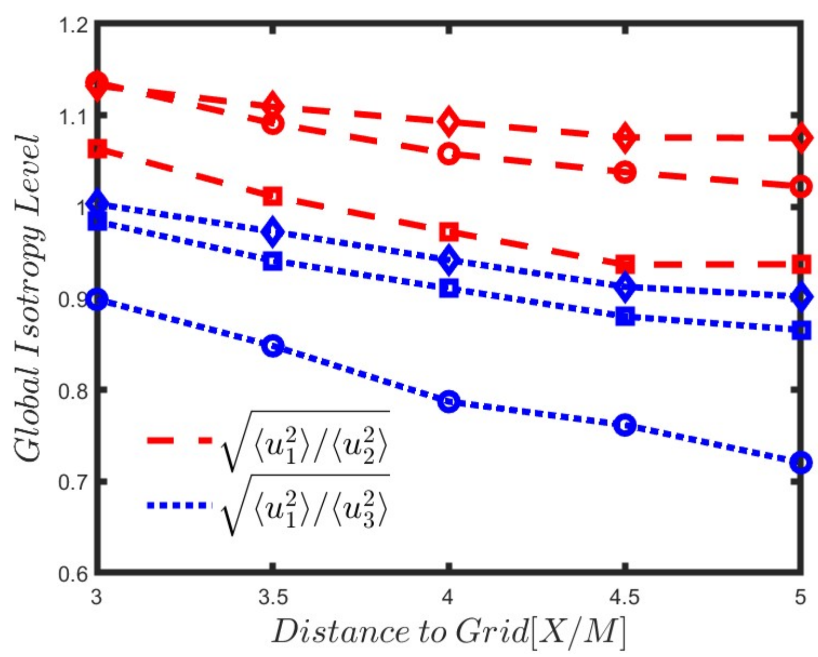

Figure 15: Global isotopry level changes over distance to grid where circle sign denotes circular winglet at $Ro_m = 23.6$,square sign denotes square winglet at $Ro_m = 23.6$ and diamons sign denotes sqaure winglet at $Ro_m = 41.8$

CHAPTER V

RESULTS

In figure 16 the velocity signal in 0.75 m distance from the active grid can be seen. Since the flow reaches this point in nearly 0.6 seconds, previous data should be ignored to not manipulate the results while making statistical calculations.

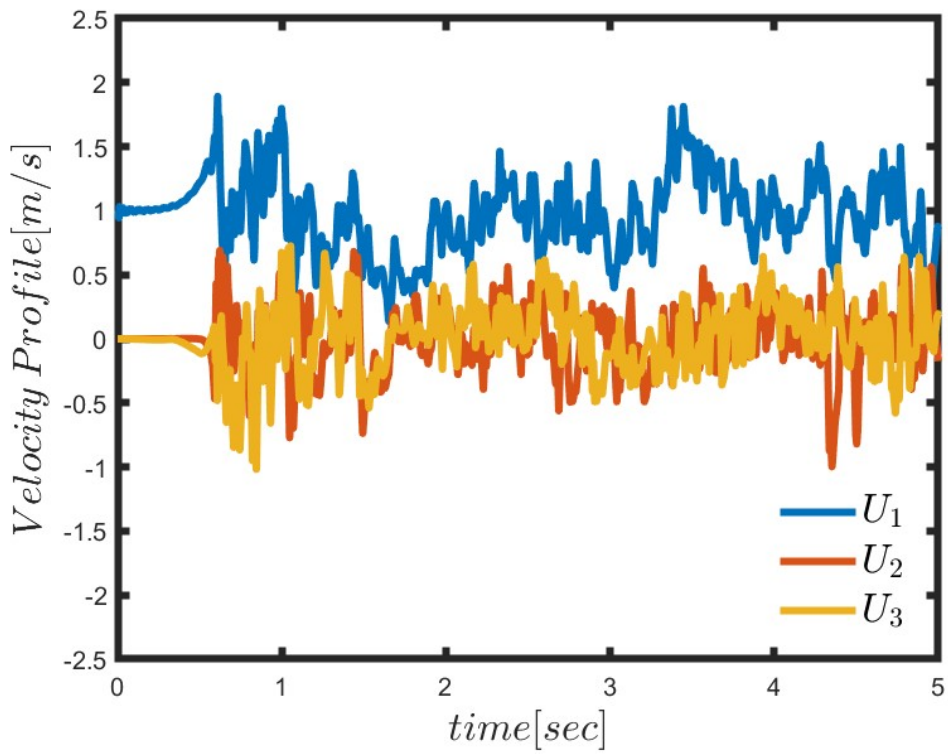

Figure 16: Three components of transient velocity signal at $X/M = 3$ with square winglets

In figures 16 and 17 the fluctuating velocity signal can be seen for 3 components. The mean velocity is extracted from the velocity signal through Reynolds decomposition. Therefore, the velocity fluctuates around 0 and the mean fluctuating velocity is 0. In the next step, the turbulent kinetic energy is calculated for several distances.

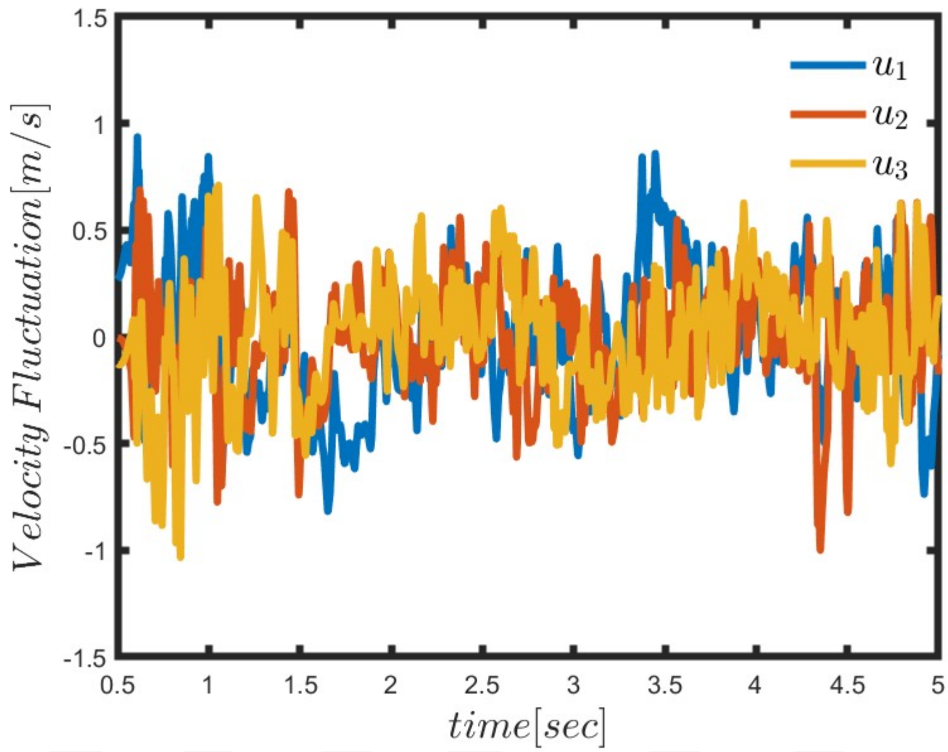

Figure 17: Three components of fluctuating velocity signal at $X/M = 3$ with square winglets

The turbulent kinetic energy can be described as[22]:

$$TKE = \frac{1}{2}[\langle u_1^2 \rangle + \langle u_2^2 \rangle + +\langle u_3^2 \rangle] \tag{29}$$

$$TKE = \frac{1}{2(N-1)} \sum_{k=1}^{N} \left[(\overline{U_{1_k}} - \langle \overline{U_{1_k}} \rangle)^2 + (\overline{U_{2_k}} - \langle \overline{U_{2_k}} \rangle)^2 + (\overline{U_{3_k}} - \langle \overline{U_{3_k}} \rangle)^2 \right] \tag{30}$$

where 1,2,3 are velocity components, U is the velocity signal, $\langle U \rangle$ is the mean velocity, and N is number of samples.

Turbulent intensity,T_q, is one of the other important parameters of turbulent results. It implies the intensity of the flow and indicates the strength of fluctuations of the flow. Turbulent intensity can be calculated with following formula[8]:

$$T_q = \frac{\langle q^2 \rangle^{\frac{1}{2}}}{3^{\frac{1}{2}} \langle U \rangle} \tag{31}$$

where $\langle q^2 \rangle$ is trace of Reynolds stress and $\langle U \rangle$ is mean velocity

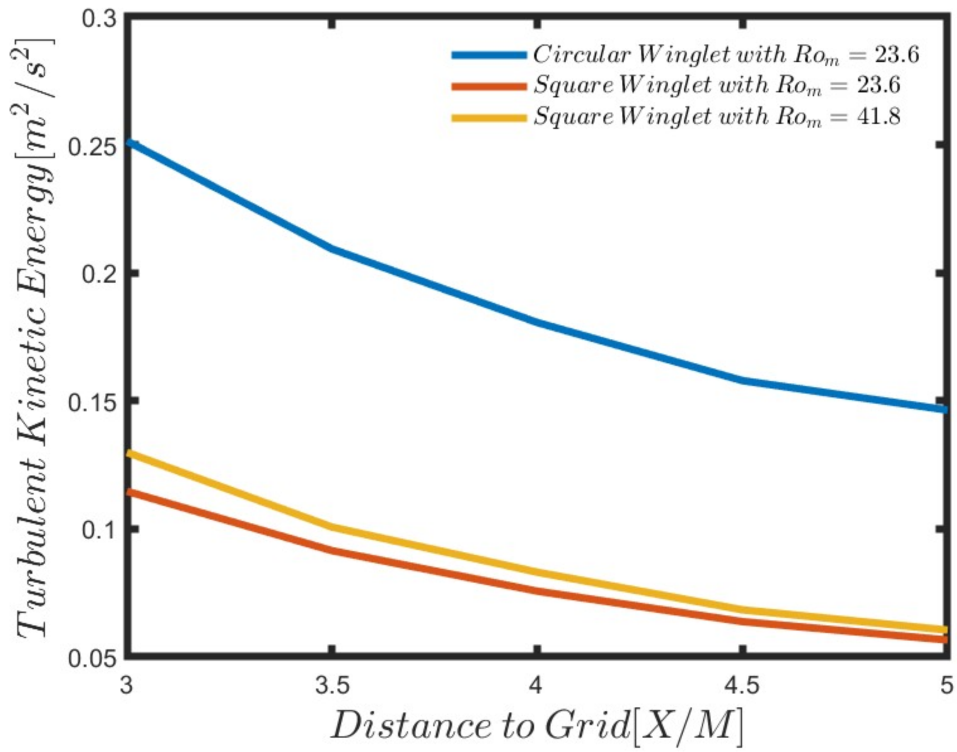

Figure 18: Surface averaged turbulent kinetic energy change for both square and circular winglets

In figure 18 turbulent kinetic energy change can be seen for both square and circular winglets. The mean turbulent kinetic energy in square and circular wings is 0.19 $\frac{m^2}{s^2}$ and 0.0805 $\frac{m^2}{s^2}$ by order. This result can be expected because of the geometry difference between the square and circular winglets.Circular winglets have more empty space between them. This space causes jet flow inside the test section. Therefore, circular wings can achieve a turbulent kinetic energy higher than that of square wings. In figure 19 turbulence intensity change can be seen. Turbulence intensity shows similar attribute with turbulent kinetic energy change.

In figure 20 the turbulent dissipation rate can be seen. The decay of turbulent kinetic energy can be examined with dissipation rate results. The mean dissipation rates for the square and circular wings are 0.084 and 0.14. The differences in the

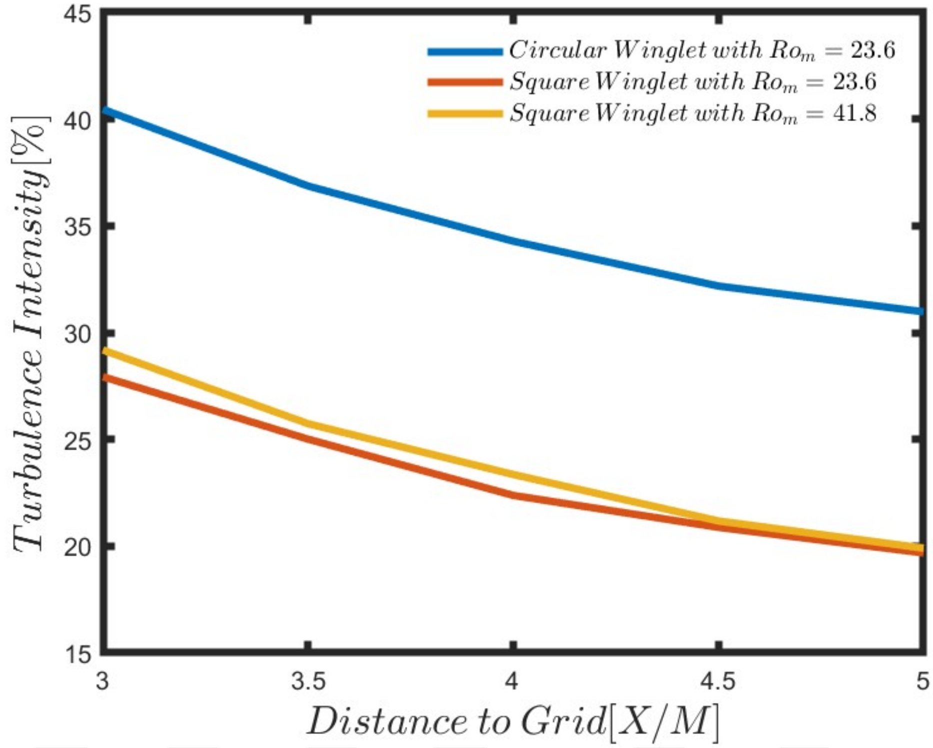

Figure 19: Surface averaged turbulence intensity change for both square and circular winglets

dissipation rate in square and circular wings are 44 % in X/M = 3 and 31% in X/M = 5. It can be observed that the difference in the decay of the turbulent kinetic energy is higher near the active grid. Therefore, the effect of jet flows can be more dominant near the active grid. One of the other main parameters of turbulent flows is the Taylor Reynolds number.Taylor Reynolds number can be calculated with two different methods. It can be calculated from both the isotropic assumption and correlation.In order to calculate Taylor Reynolds number from the isotropic assumption, the Taylor microscale has to be calculated. Taylor microscale,λ_g, can be calculated by following the formula [15];

$$\frac{{\lambda_g}^2}{\langle q^2 \rangle} = \frac{5\nu}{\epsilon} \tag{32}$$

In addition, the Taylor microscale can be calculated from the autocorrelation of

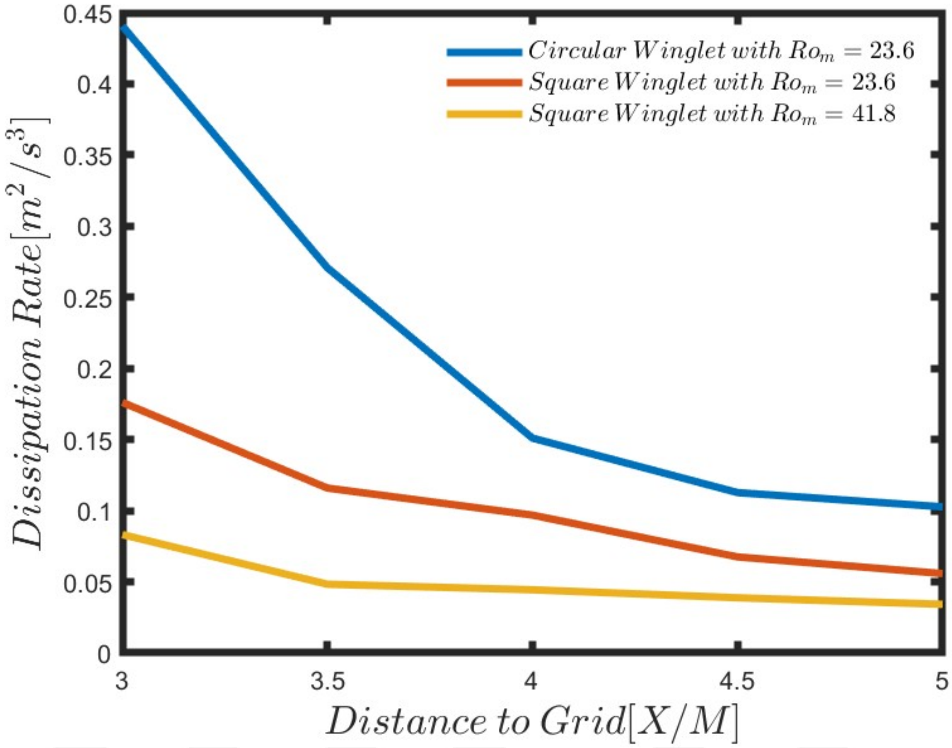

Figure 20: Surface averaged turbulence dissipation rate change for square and circular winglet

flow. Autocorrelation function,$R_{22}(x_1)$, can be calculated with the following following formula:

$$R_{22}(x_1) = \frac{\overline{u_2'(0)u_2'(x_1)}}{u_2'(0)u_2'(0)} \tag{33}$$

Then, the Taylor microscale and Taylor Reynolds number can be calculated with the following following formula:

$$-2\frac{1}{\lambda_g^2} = (\frac{\partial^2 R_{22}(x_1)}{\partial^2 x_1})_{x_2=0} \tag{34}$$

$$Re_\lambda = \sqrt{\frac{\langle q^2 \rangle}{3}}\frac{\lambda_g}{\nu} \tag{35}$$

In figure 21 Taylor Reynolds number can be seen. Taylor Reynolds number calculated with two different methods, the isotropic assumption and correlation. There is

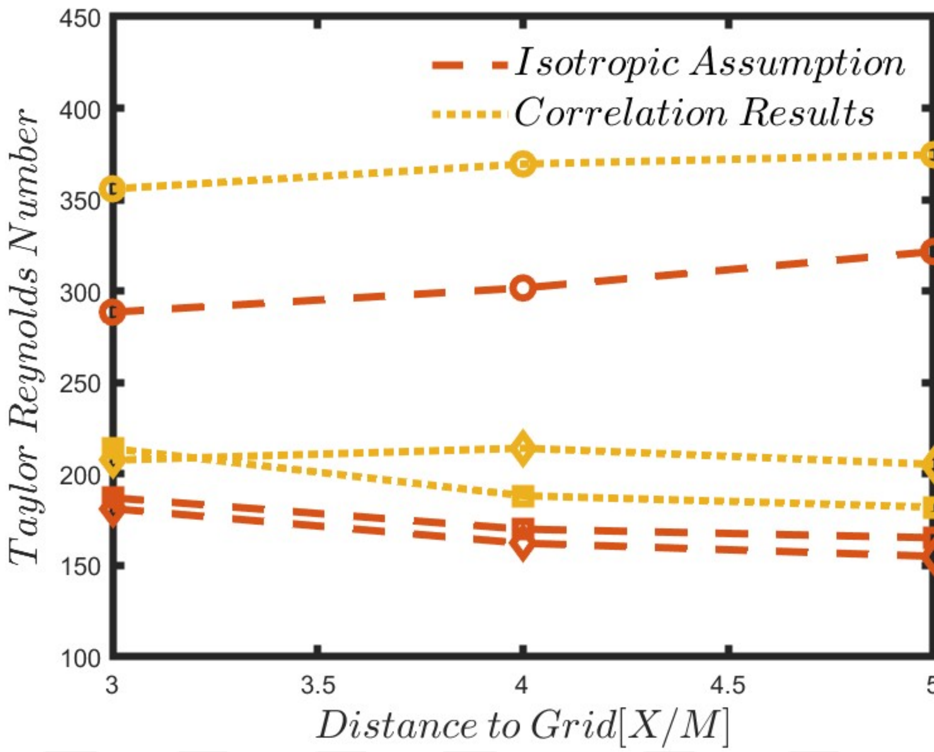

Figure 21: Taylor Reynolds number change where circle sign denotes circular winglet at $Ro_M = 23.6$,square sign denotes square winglet at $Ro_M = 23.6$ and diamons sign denotes sqaure winglet at $Ro_M = 41.8$

a difference between the results.In correlation-dependent Taylor Reynolds numbers, the velocity signal from the point probe is used. In isotropic assumptions, surface-averaged Reynolds stresses are used. Therefore, it is expected to have a difference between them. To obtain more close results, several point probes can be placed and averaged. In circular winglets, nearly 350 Re_λ achieved. In square winglets, 150-200 Re_λ achieved. In $Ro_M = 41.8$ higher Re_λ is achieved.

In next section, the power spectrum of velocity signals is compared with each other. The one-dimensional energy spectrum can be expressed as:

$$a_{u_j}(f) = \int_0^T u_j'(t)e^{-i2\pi ft}dt \tag{36}$$

$$E_{u_j}(f)) = \frac{2}{T}|a_{u_j}(f)|^2 \tag{37}$$

where j = 1,2,3 which demonstrate direction.

The velocity signal is converted into various frequencies.Spectrum can be expressed in wave number form with the following formulation[23]:

$$k = \frac{2\pi f}{\langle U \rangle} \tag{38}$$

$$E_{u_j}(k) = \frac{\langle U \rangle}{2\pi} E_{u_j}(f) \tag{39}$$

Also, a one-dimensional spectrum can be converted into a three-dimensional spectrum with the following formula[22]:

$$k_{3d}^2 = \sum_{j=1}^{3} k_j^2 \tag{40}$$

$$E_1(k_{3d})^2 = \sum_{j=1}^{3} E_{u_j}(k)^2 \tag{41}$$

The validation of the spectrum can be confirmed by the calculation of kinetic energy using the following formula:

$$\frac{1}{2}\int E_1(k_{3d})dk_{3d} = \frac{1}{2}[\langle u_1'^2 \rangle + \langle u_2'^2 \rangle + \langle u_3'^2 \rangle] \tag{42}$$

In figures 22, 23 and 24 the $E_1(k_{3d})$ can be seen in different winglets and motion protocols. All spectrums are following $k^{-5/3}$ line in wavenumber space until cutoff wavenumber based on mesh size.This limit is defined with $\frac{U}{\Delta x}$.Then converted in wavenumber with equation (38).All of the spectra show the existence of the inertial subrange because the spectra follow $k^{-5/3}$ line in wave number space. The area under the three-dimensional spectrum is related to the turbulent kinetic energy as mentioned in eq (42). Therefore, while the distance from the winglets is increased, the $E_1(k_{3d})$ decreases.

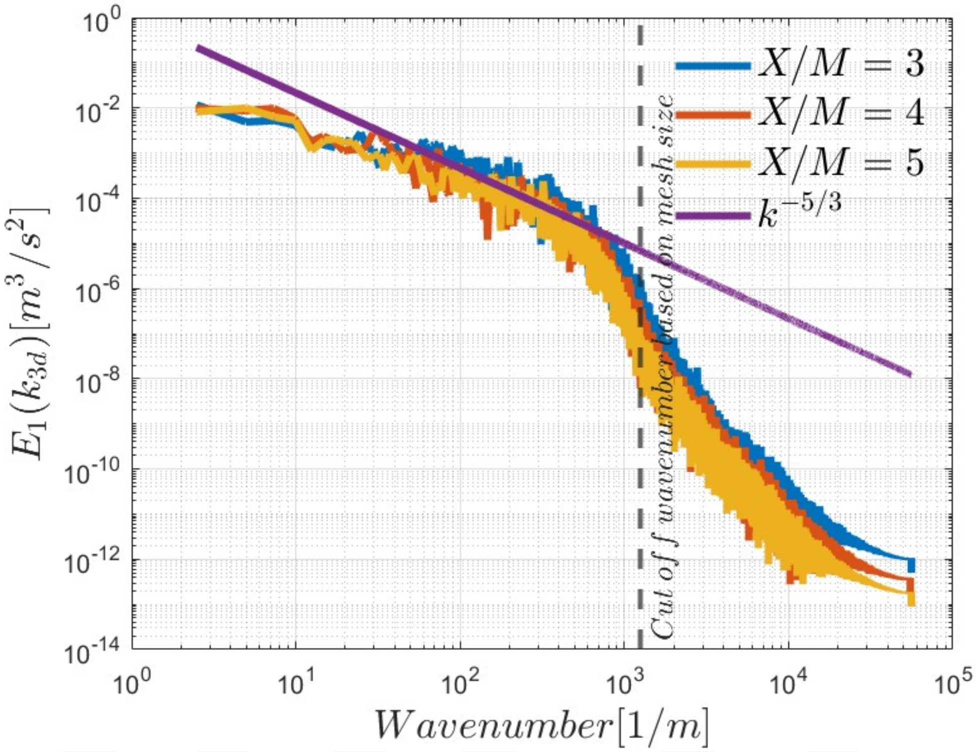

Figure 22: Variation of $E_1(k_{3d})$ of turbulence along the flow for square winglet at $Ro_M = 23.6$

As mentioned before circular winglets provide quite higher levels of turbulence. Space between circular winglets can create jet flows. Therefore, homogeneity of velocity and turbulent kinetic energy is calculated and visualized in both x-y and x-z planes. Homogenity can be calculated with following formula:

$$I_{\langle H \rangle}(x_1, x_2) = \frac{\langle H \rangle(i\Delta x_1, j\Delta x_2) - \frac{1}{N_{x_2}}\frac{1}{N_{x_3}}\sum_{k=1}^{N_{x2}}\sum_{m=1}^{N_{x3}} \langle H \rangle(i\Delta x_1, k\Delta x_2, m\Delta x_3)}{\left|\frac{1}{N_{x_2}}\frac{1}{N_{x_3}}\sum_{k=1}^{N_{x2}}\sum_{m=1}^{N_{x3}} \langle H \rangle(i\Delta x_1, k\Delta x_2, m\Delta x_3)\right|} \tag{43}$$

where $I_{\langle H \rangle}(x_1, x_2)$ is inhomogeneity parameter,Δx_1 Δx_2 Δx_3 are resolution in three direction,N_{x_1} is points in flow direction,N_{x_2} and N_{x_3} are points in transverse direction , $\langle H \rangle$ is mean of any quantity such as velocity. Homogeneity is calculated for both turbulent kinetic energy and velocity in upstream direction. When different motion protocols are compared, $Ro_M = 23.6$ causes more inhomogeneous flow rather

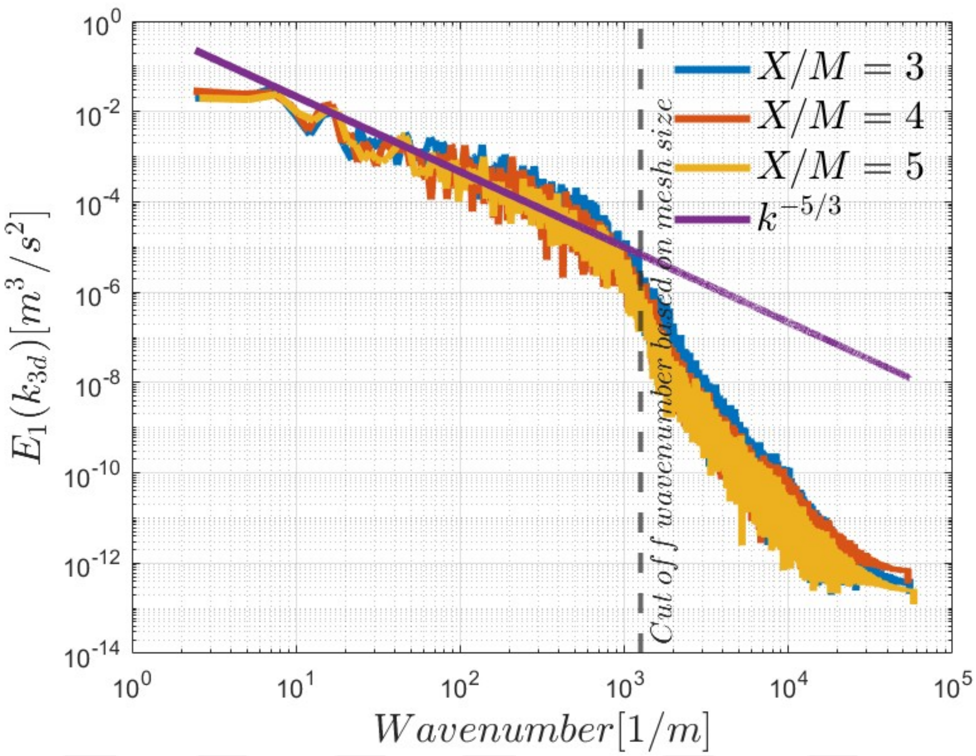

Figure 23: Variation of $E_1(k_{3d})$ of turbulence along the flow for circular winglet at $Ro_M = 23.6$

than $Ro_M = 41.8$. This attribute can be observed in both $I_{\langle TKE \rangle}$ and $I_{\langle U_1 \rangle}$. Hence, higher Rossby number causes lower homogeneity level.Also, circular winglets causes more inhomogeneous flow. In figure 37 probability density function of velocity in upstream direction is calculated for all cases. In figure 37 square winglets with $Ro_M = 41.8$ has the highest peak at $I_{\langle U_1 \rangle} = 0$ which means it is the most homogeneous flow between them.In contrast circular winglets with $Ro_M = 23.6$ is the least homogeneous flow. This attribute caused by 2 different reasons.First shapes of circular winglets can create more jet flows than square winglets. Also, in figure 5 circular winglets can close higher area with same motion protocol.

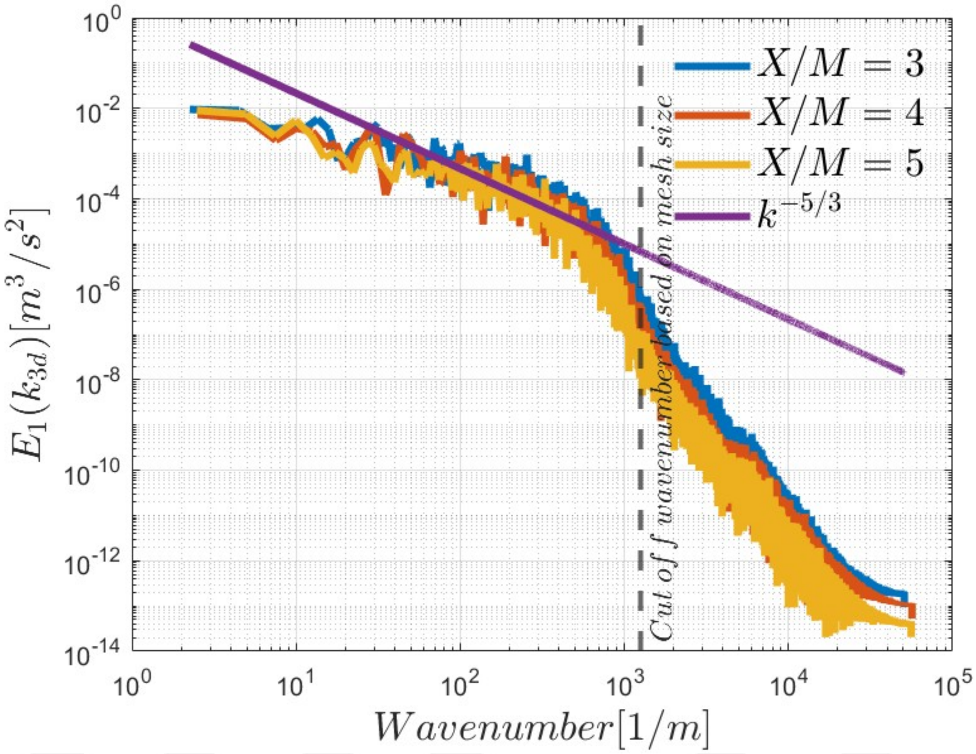

Figure 24: Variation of $E_1(k_{3d})$ of turbulence along the flow for square winglet at $Ro_M = 41.8$

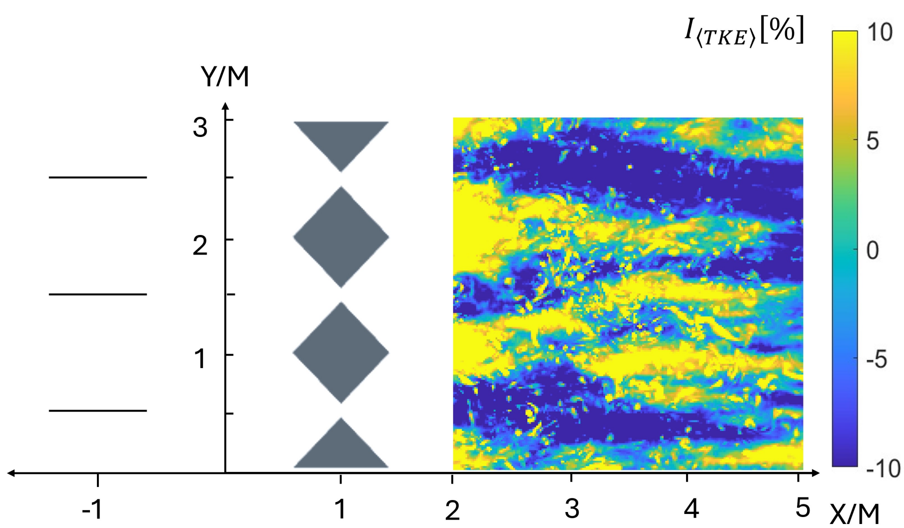

Figure 25: Homogeneity of turbulent kinetic energy for $Ro_M = 23.6$ and square winglet in xy plane

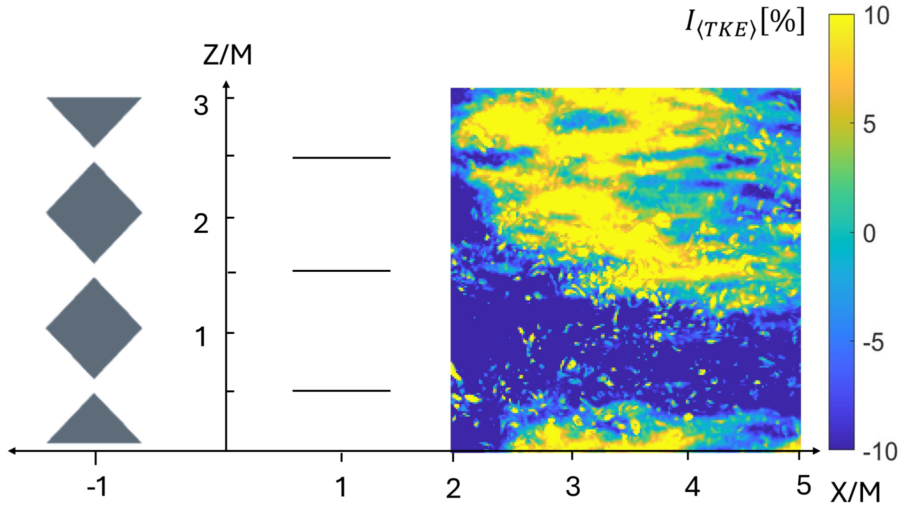

Figure 26: Homogeneity of turbulent kinetic energy for $Ro_M = 23.6$ and square winglet in xz plane

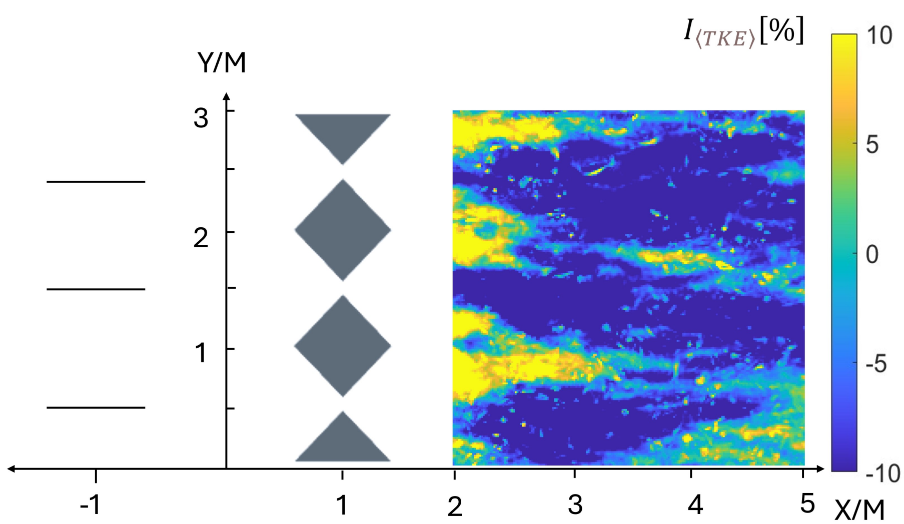

Figure 27: Homogeneity of turbulent kinetic energy for $Ro_M = 41.8$ and square winglet in xy plane

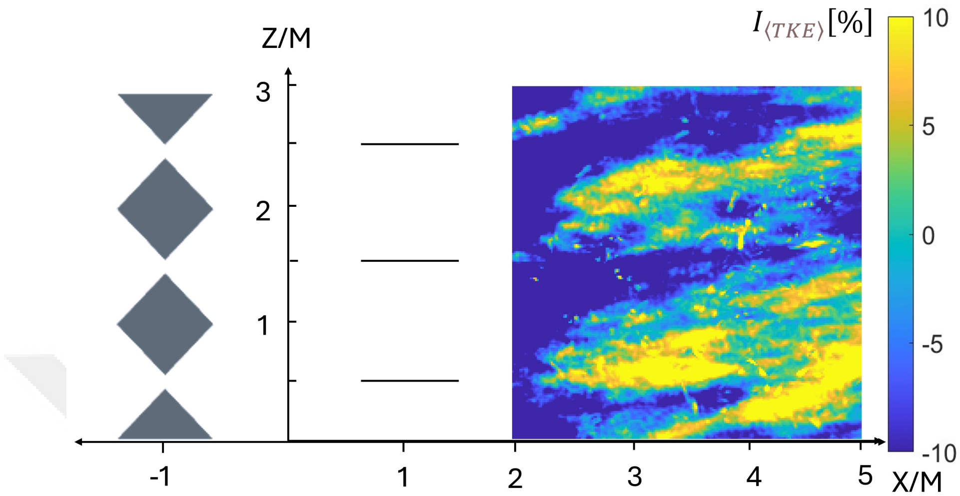

Figure 28: Homogeneity of turbulent kinetic energy for $Ro_M = 41.8$ and square winglet in xz plane

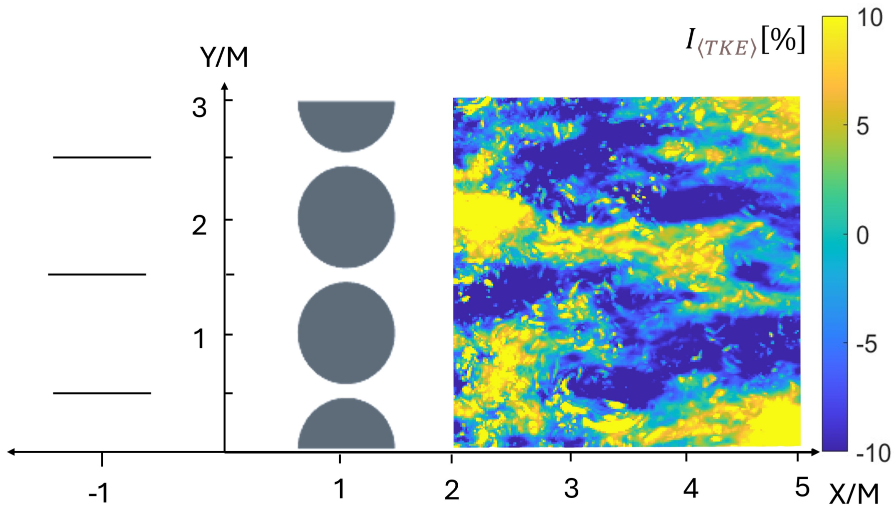

Figure 29: Homogeneity of turbulent kinetic energy for $Ro_M = 23.6$ and circular winglet in xy plane

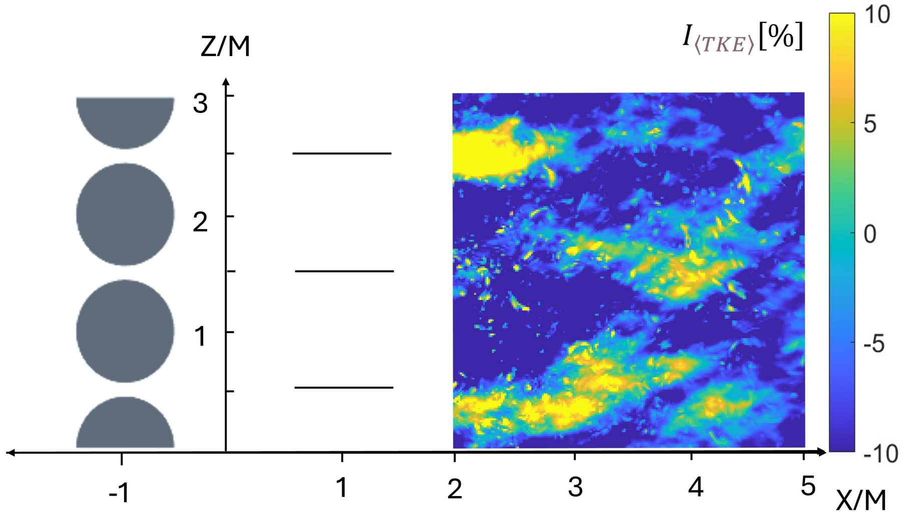

Figure 30: Homogeneity of turbulent kinetic energy for $Ro_M = 23.6$ and circular winglet in xz plane

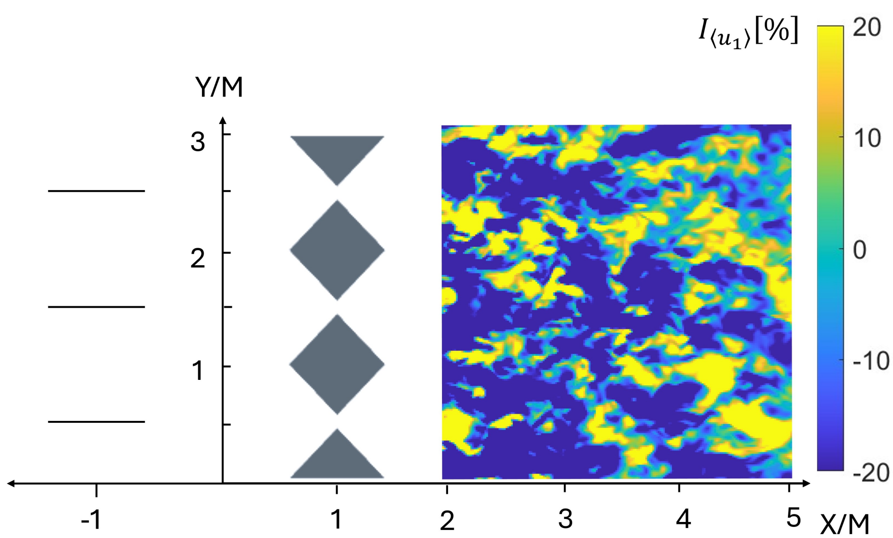

Figure 31: Homogeneity of u_1 for $Ro_M = 23.6$ and square winglet in xy plane

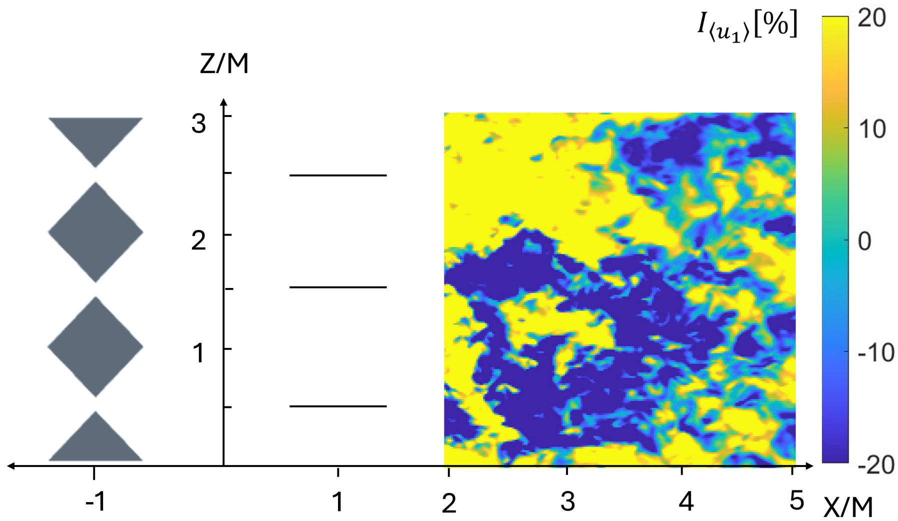

Figure 32: Homogeneity of u_1 for $Ro_M = 23.6$ and square winglet in xz plane

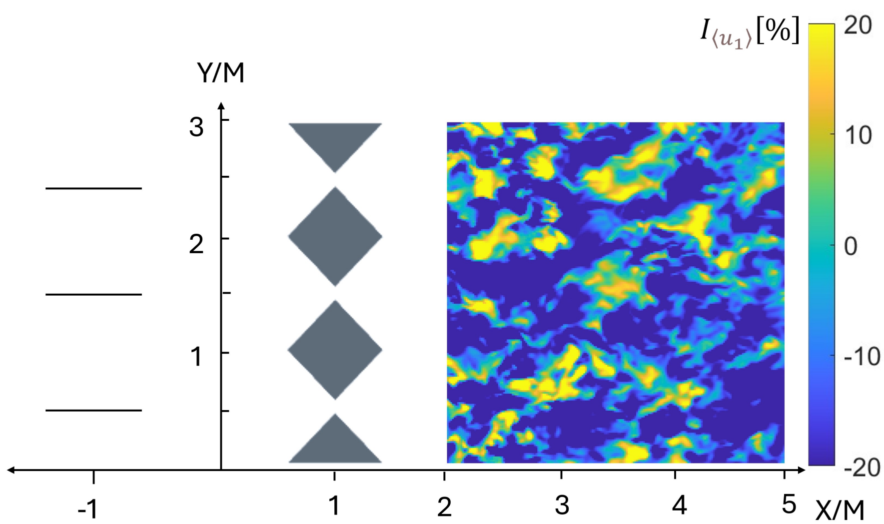

Figure 33: Homogeneity of u_1 for $Ro_M = 41.8$ and square winglet in xy plane

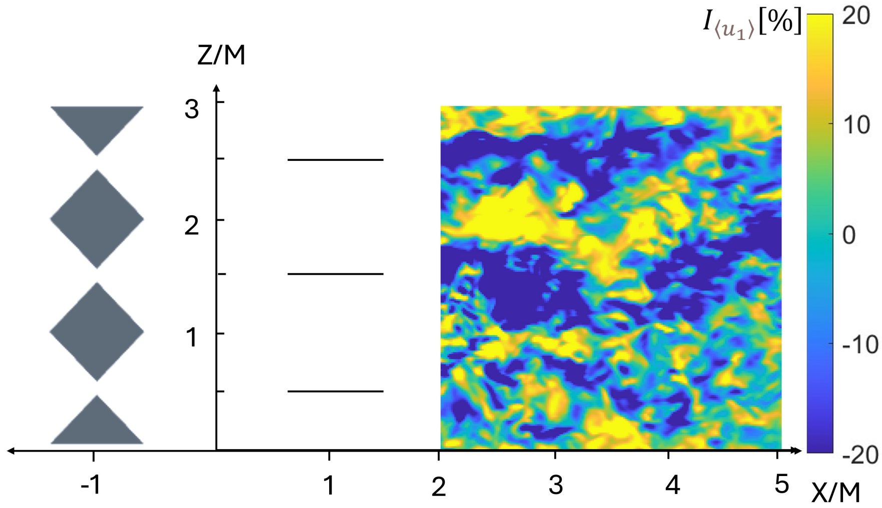

Figure 34: Homogeneity of u_1 for $Ro_M = 41.8$ and square winglet in xz plane

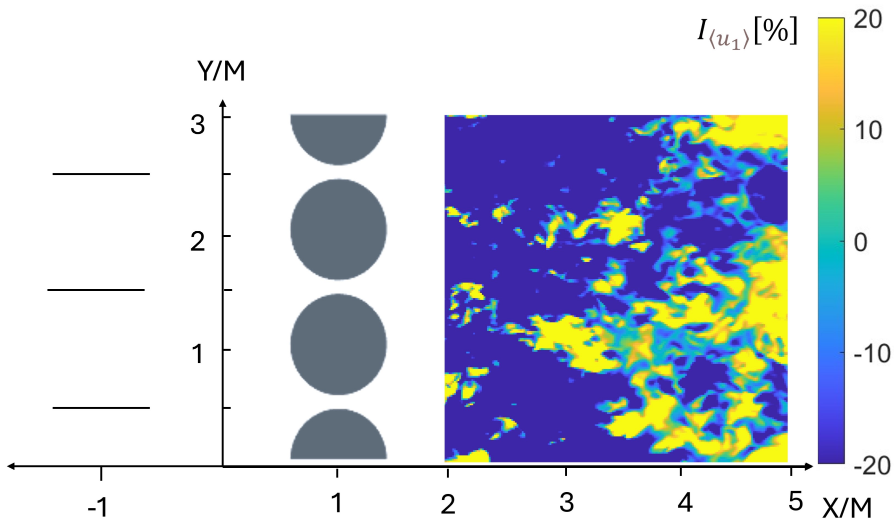

Figure 35: Homogeneity of u_1 for $Ro_M = 23.6$ and circular winglet in xy plane

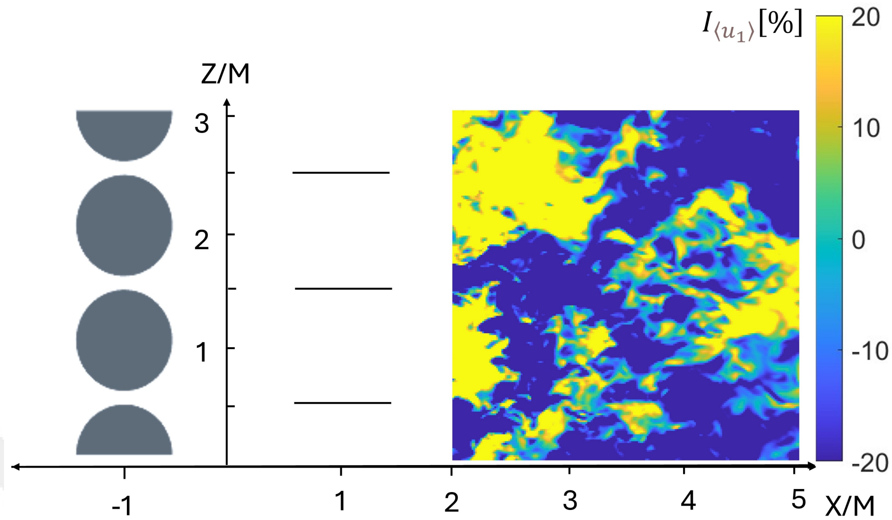

Figure 36: Homogeneity of u_1 for $Ro_M = 23.6$ and circular winglet in xz plane

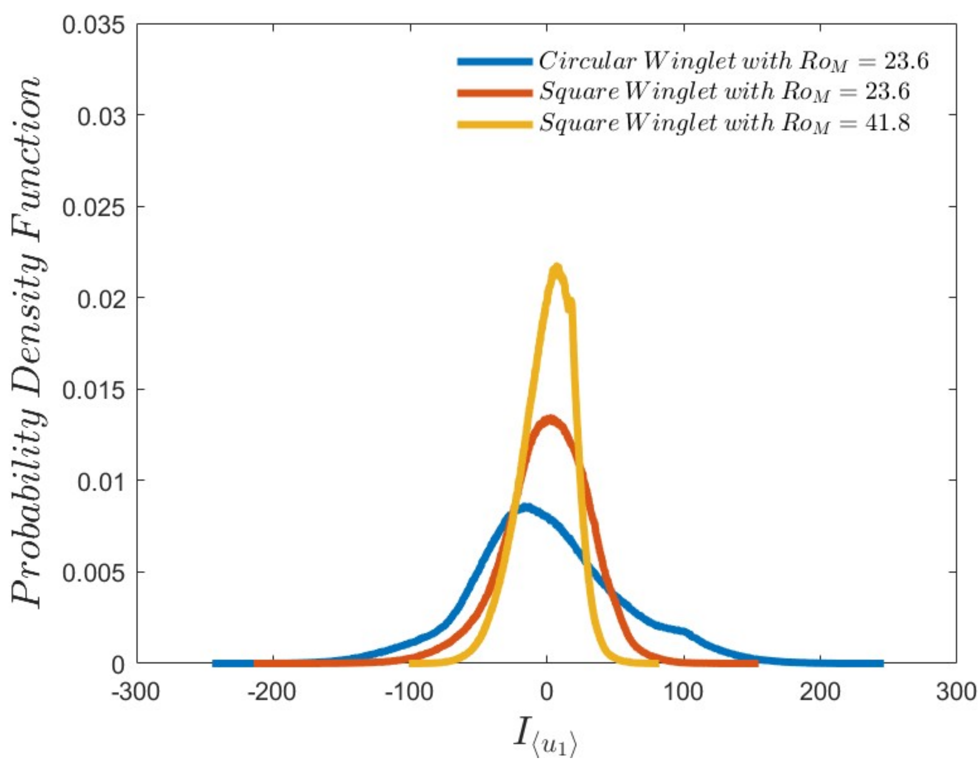

Figure 37: Probablity density function of velocity homogenity for different motion protocols and winglets

CHAPTER VI

CONCLUSIONS

This paper details the study on winglet shape effects and the proposed motion protocol using Large Eddy Simulation. The simulation runs in Star-CCM+, a very robust commercial software in computational fluid dynamics. Several methods were applied for checking the accuracy of the results obtained from the simulation, hence proving a high degree of reliability.First, the resolved kinetic energy and the resolved dissipation rate were tested. Both these parameters are crucial in determining how well the Sub-Grid Scale models applied within the LES worked. The mean values for resolved turbulent kinetic energy and resolved turbulent dissipation rate is 95% and 60%. For further validation of the accuracy of the simulations, the quality indices were checked with respect to the LES quality index (LES$_{IQ}$) and the Courant number. This value was found to be below 0.5 over most of the domain, amounting to stable and accurate simulation.LES_{IQ} was above 90% everywhere, except for local drops, due to an increasing velocity at the winglet tips. In such complex flow situations, this must be expected.

In the next step, isotropy of the flow is tested with both global isotropy level.Isotropy is very important for most of the aerodynamic applications and refers to the uniformity of turbulence in all directions. The values of square winglets can be accepted within the isotropic range, while the values of the circular winglets are at the limit of this range. This means that the geometry of the winglets plays a very important role in deciding on the isotropy of the turbulence that is generated.

The study has also examined the effect of different motion protocols on the kinetic energy and turbulence intensity. The comparison was made between two different motion protocols applied: $Ro_m = 41.8$ and $Ro_m = 23.6$. The results showed that $Ro_m = 41.8$ gave approximately 8% more turbulent kinetic energy and turbulence intensity compared to $Ro_m = 23.6$.Hearst and Lavoie[8] show similir effect in their study. Increase in Ro number causes higher turbulent kinetic energy and turbulent intensity. It is observed, compared with square winglets, the magnitude of turbulent kinetic energy and turbulence intensity with circular winglets is almost twice as big. That means circular winglets are more efficient in enhancing turbulence.Taylor microscale Reynolds number, Re_λ, show the similar increase as well. For $Ro_m = 41.8$ and $Ro_m = 23.6$ square winglets gave values of almost 250, while for circular winglets returned a value of around 350 for Re_λ. So, circular winglets perform lots better in creating higher-intensity turbulence.

The homogeneity results show that circular winglets are more inhomogeneous compared to square winglets. Inhomogenity is related to the mean closure of the active grid. In figure 5 circular winglets have a higher mean closure than square winglets. Therefore, they can create jet flows and create more inhomogeneous flow. It is important to note that the circular winglets provided higher levels of turbulence but in trade off reduced isotropy and homogeneity. However, this presents a fundamental trade-off in those few applications where isotropy and homogeneity matter much.

In the thesis, effect of motion protocols have a major contribution. The objective was to control the closure over time while creating a high level of turbulence with controlling intensity of closure and Ro_m. Intensity of closure keep remain and effect of Ro_m is examined. It is expected to achieve a high level of turbulence with a higher number Ro. The turbulent kinetic energy, turbulent intensity and the Re_λ results show this effect. In addition, the effect of mean closure was examined. Higher mean closure can create higher level of turbulence in trade off reduced homogenity.

To conclude, thesis has exhaustively looked at the effect of winglet shape and motion protocol on turbulent flow characteristics using LES. The results bring into attention the central role played by the winglet design in determining the turbulence levels, isotropy, and homogeneity documented. Even though winglets of the circular shape develop much more turbulence, they are not suitable for problems with high isotropy. In these cases, one could prefer the winglet of the square shape since it performs more uniformly.Future studies could focus on the optimization of winglet designs to achieve a better balance between turbulence generation and isotropy. This study can be expanded to improve the understanding of the dynamics by changing the flow conditions and setups. Finally, the work can be considered as a contribution to the large body of experience in the aerodynamic design and turbulence modeling communities, paving the way toward better-engineered solutions with more efficiency.

APPENDIX A

APPENDIX 1

```

options = optimoptions("gamultiobj","PlotFcn","gaplotpareto
    ",...
"PopulationSize",5000,'MaxGenerations',20,'ParetoFraction'
    ,0.3,'UseParallel',true);
[x fval]= gamultiobj(@two_layer_op,12,[],[],[],[],lb,ub,
    options);

function Output = two_layer_op(Input)
x1 = Input(1);
x2 = Input(2);
x3 = Input(3);
x4 = Input(4);
x5 = Input(5);
x6 = Input(6);
x7 = Input(7);
x8 = Input(8);
x9 = Input(9);
x10 = Input(10);
x11 = Input(11);
x12 = Input(12);
Free_Stream_Velocity = 1;
dt = 0.01;
```

```
time = 0:dt:10;
M = 0.15;
flapping2 = (pi/2) + (0.275*pi)*sin(2*pi*x3*(time))+(0.275*pi)
    *sin(2*pi*x4*(time)); %rad
flapping4 = (pi/2) + (0.275*pi)*sin(2*pi*x7*(time))+(0.275*pi)
    *sin(2*pi*x8*(time)); %rad
flapping6 = (pi/2) + (0.275*pi)*sin(2*pi*x11*(time))+(0.275*pi
    )*sin(2*pi*x12*(time)); %rad


flapping1 = (0.275*pi)*sin(2*pi*x1*time)+(0.275*pi)*sin(2*pi*
    x2*time); %rad
flapping3 = (0.275*pi)*sin(2*pi*x5*(time))+(0.275*pi)*sin(2*pi
    *x6*(time)); %rad
flapping5 = (0.275*pi)*sin(2*pi*x9*(time))+(0.275*pi)*sin(2*pi
    *x10*(time)); %rad



for j = 1:length(time)-1
    vel1(j) = (flapping1(j+1) - flapping1(j))/dt; %rad/s
    vel2(j) = (flapping2(j+1) - flapping2(j))/dt; %rad/s
    vel3(j) = (flapping3(j+1) - flapping3(j))/dt; %rad/s
    vel4(j) = (flapping4(j+1) - flapping4(j))/dt; %rad/s
    vel5(j) = (flapping5(j+1) - flapping5(j))/dt; %rad/s
    vel6(j) = (flapping6(j+1) - flapping6(j))/dt; %rad/s
end
```

```
for k=1:length(time)
Area = ((106.066*10^-3)^2);
Domain_Area = 0.52*0.52;
    Rod1_pro(k) = abs(sin(flapping1(k)));
    Rod2_pro(k) = abs(sin(flapping2(k)));
    Rod3_pro(k) = abs(sin(flapping3(k)));
    Rod4_pro(k) = abs(sin(flapping4(k)));
    Rod5_pro(k) = abs(sin(flapping5(k)));
    Rod6_pro(k) = abs(sin(flapping6(k)));
    tot_pro(k) = 3*Area*(Rod1_pro(k) +Rod2_pro(k) +Rod3_pro(k) +Rod4_pro(k) +Rod5_pro(k) +Rod6_pro(k));
    closure(k) = (tot_pro(k)/Domain_Area)*100;
end
mean_vel1 = mean(abs(vel1))/(2*pi); %Hz
mean_vel2 = mean(abs(vel2))/(2*pi); %Hz
mean_vel3 = mean(abs(vel3))/(2*pi); %Hz
mean_vel4 = mean(abs(vel4))/(2*pi); %Hz
mean_vel5 = mean(abs(vel5))/(2*pi); %Hz
mean_vel6 = mean(abs(vel6))/(2*pi); %Hz
Ro1 = Free_Stream_Velocity/(M*mean_vel1);
Ro2 = Free_Stream_Velocity/(M*mean_vel2);
Ro3 = Free_Stream_Velocity/(M*mean_vel3);
Ro4 = Free_Stream_Velocity/(M*mean_vel4);
Ro5 = Free_Stream_Velocity/(M*mean_vel5);
Ro6 = Free_Stream_Velocity/(M*mean_vel6);
Rossby = [Ro1 Ro2 Ro3 Ro4 Ro5 Ro6];
Average_Rossby = (Ro1+ Ro2+ Ro3+ Ro4+ Ro5+ Ro6)/6;
absclosure = abs(closure);
Desired_Rossby = 25;
```

```
intensity_of_closure = 0.075;
res1 = abs(intensity_of_closure - std(absclosure)/mean(
    absclosure));
res2 = abs(Desired_Rossby - Average_Rossby);
Output = [res1 res2 res3];
end
```

Listing A.1: Generating Motion Protocol wiht MATLAB

APPENDIX B

APPENDIX 2

```
%% Power Spectrum
veldata= readmatrix('Velocities.xlsx');
time= veldata([5000:50000],1);  %time
dt = time(2) - time(1);
v = 1.48 * 10^-5; %kinematic viscosity of Air
size = [5000:50000];
for i = 1:9
    mean_velocity(:,i) = mean(veldata([size],i+1));
    fluc(:,i) =  veldata([size],i+1) - mean_velocity(:,i);
end


pack = 45000;
fs = 1/dt;
[powU1_i,ff1_i]= pwelch(fluc(:,1),[pack],[pack/2],[pack],fs);
[powU1_j,ff1_j]= pwelch(fluc(:,2),[pack],[pack/2],[pack],fs);
[powU1_k,ff1_k]= pwelch(fluc(:,3),[pack],[pack/2],[pack],fs);


k1_i = (2*pi*ff1_i)/mean_velocity(1);  %wavenumber
k1_j = (2*pi*ff1_j)/mean_velocity(1);
k1_k = (2*pi*ff1_k)/mean_velocity(1);
powk1_i=(mean_velocity(1)/(2*pi))*powU1_i;
```

```
powk1_j=(mean_velocity(1)/(2*pi))*powU1_j;
powk1_k=(mean_velocity(1)/(2*pi))*powU1_k;
for i = 1:length(k1_i)
    k_1_3d(i) = sqrt(k1_i(i)^2 + k1_j(i)^2 + k1_k(i)^2);
    powk1_3d(i) = sqrt(powk1_i(i)^2 + powk1_j(i)^2 + powk1_k(i)^2);
end
for i = 1:length(k1_i)
    ff_1_3d(i) = sqrt(ff1_i(i)^2 + ff1_j(i)^2 + ff1_k(i)^2);
    powU1_3d(i) = sqrt(powU1_i(i)^2 + powU1_j(i)^2 + powU1_k(i)^2);
end
```

Listing B.1: Power Spectrum Calculation wiht MATLAB

REFERENCES

[1] G. Comte-Bellot and S. Corrsin, "The use of a contraction to improve the isotropy of grid-generated turbulence," *Journal of Fluid Mechanics*, vol. 25, p. 657–682, Aug 1966.

[2] A. Thormann and C. Meneveau, "Decay of homogeneous, nearly isotropic turbulence behind active fractal grids," *Physics of Fluids*, vol. 26, 1 2014.

[3] P. C. Valente and J. C. Vassilicos, "The non-equilibrium region of grid-generated decaying turbulence," *Journal of Fluid Mechanics*, vol. 744, pp. 5–37, 2014.

[4] P. D'Addio, D. Sassun, O. Flores, and P. Orlandi, "Influence of solid boundary conditions on the evolution of free and wall-bounded turbulent flows," *Journal of Physics: Conference Series*, vol. 506, no. 1, 2014.

[5] Ö. Ertunç, N. Özyilmaz, H. Lienhart, F. Durst, and K. Beronov, "Homogeneity of turbulence generated by static-grid structures," *Journal of Fluid Mechanics*, vol. 654, pp. 473–500, 2010.

[6] H. Makita, "Realization of a large-scale turbulence field in a small wind tunnel," *Fluid Dynamics Research*, vol. 8, pp. 53–64, 1991.

[7] N. Reinke, T. Homeyer, M. Hölling, and J. Peinke, "Flow Modulation by an Active Grid," no. March, 2017.

[8] R. J. Hearst and P. Lavoie, "The effect of active grid initial conditions on high Reynolds number turbulence," *Experiments in Fluids*, vol. 56, no. 10, 2015.

[9] T. Skeledzic, J. Krauss, H. Lienhart, Ertunc, and J. Jovanovic, "Characterization of turbulence generated by an active grid with individually controllable paddles," *Notes on Numerical Fluid Mechanics and Multidisciplinary Design*, vol. 136, pp. 105–114, 2018.

[10] H. S. Kang, S. Chester, and C. Meneveau, "Decaying turbulence in an active-grid-generated flow and comparisons with large-eddy simulation," *Journal of Fluid Mechanics*, vol. 480, no. 480, pp. 129–160, 2003.

[11] K. P. Griffin, N. J. Wei, E. Bodenschatz, and G. P. Bewley, "Control of long-range correlations in turbulence," *Experiments in Fluids*, vol. 60, no. 4, pp. 617–639, 2019.

[12] L. Neuhaus, F. Berger, J. Peinke, and M. Hölling, "Exploring the capabilities of active grids," *Experiments in Fluids*, vol. 62, pp. 1–13, 2021.

[13] G. P. Bewley, J. Kassel, and E. Bodenschatz, "Control of turbulence with a high degree-of-freedom active grid," *ETC 2013 - 14th European Turbulence Conference*, pp. 4–5, 2020.

[14] L. Mydlarski and Z. Warhaft, “On the onset of high-Reynolds-number grid-generated wind tunnel turbulence,” *Journal of Fluid Mechanics*, vol. 320, pp. 331–368, 1996.

[15] S. B. Pope, *Turbulent flows*. Cambridge University Press, 2000.

[16] A. G. Gungor and S. Menon, “A new two-scale model for large eddy simulation of wall-bounded flows,” *Progress in Aerospace Sciences*, vol. 46, no. 1, p. 28–45, 2010.

[17] R. A. Clark, J. H. Ferziger, and W. C. Reynolds, “Evaluation of subgrid-scale models using an accurately simulated turbulent flow,” *Journal of Fluid Mechanics*, vol. 91, no. 01, p. 1, 1979.

[18] G. Alfonsi, “Reynolds-averaged navier-stokes equations for turbulence modeling,” *Applied Mechanics Reviews*, 2009.

[19] F. Nicoud and F. Ducros, “Subgrid-scale stress modelling based on the square of the velocity gradient tensor,” 1999.

[20] R. Bhaskaran and L. Collins, “Introduction to cfd basics,” *Cornell University-Sibley School of Mechanical and Aerospace Engineering*, pp. 1–21, 2002.

[21] I. B. Celik, Z. N. Cehreli, and I. Yavuz, “Index of resolution quality for large eddy simulations,” *Journal of Fluids Engineering, Transactions of the ASME*, vol. 127, pp. 949–958, 2005.

[22] W. K. George, “Lectures in turbulence for the 21st century, imperial college of london and chalmers university of technology,” *Website*, p. 351, 2013.

[23] Ertunç, “Experimental and numerical investigations of axisymmetric turbulence,” pp. 1–236, 2006.

VITA

Alper Akardere graduated from Beşiktaş Atütürk Anatolian High School. Bachelor's degree is received from Özyeğin University in mechanical engineering at 2021. Also, master's degree is obatined from Özyeğin University with supervision of Assoc.Prof.Dr.-Ing. Özgür Ertunç. Main research areas are turbulent flows and LES simulations.